Chemical and Geometric Transformations of MoS_2/WS_2 Heterostructures by Plasma Treatment

By

Mu-Tao Chen

A Thesis Presented in Partial Fulfillment
of the Requirements for the Degree
Master of Science

Approved November 2019 by the
Graduate Supervisory Committee:

Qing Hua Wang, Chair
Alexander Green
Yu Yao

ARIZONA STATE UNIVERSITY

December 2019

ABSTRACT

Two-dimensional (2D) transition metal dichalcogenides (TMDCs) like molybdenum disulfide (MoS_2) and tungsten disulfide (WS_2) are effective components in optoelectronic devices due to their tunable and attractive electric, optical and chemical properties. Combining different 2D TMDCs into either vertical or lateral heterostructures has been pursued to achieve new optical and electronic properties. Chemical treatments have also been pursued to effectively tune the properties of 2D TMDCs. Among many chemical routes that have been studied, plasma treatment is notable for being rapid and versatile. In Wang's group earlier work, plasma treatment of MoS_2 and WS_2 resulted in the formation of MoO_3 and WO_3 nanosheets and nanoscrolls. However, plasma treatment of 2D TMDC heterostructures have not been widely studied. In this dissertation, MoS_2/WS_2 vertical and lateral heterostructures were grown and treated with air plasma. The result showed that the vertical heterostructure and lateral heterostructures behaved differently. For the vertical heterostructures, the top WS_2 layer acts as a shield for the underlying MoS_2 monolayer from oxidizing and forming transition metal oxide nanoscrolls, as shown by Raman spectroscopy and atomic force microscopy (AFM). On the contrary, for the lateral heterostructures, the WS_2 that was grown surrounding the MoS_2 triangular core served as a tight frame to stop the propagation of the oxidized MoS_2, resulting a gradient of crack distribution. These findings provide insight into how plasma treatment can affect the formation of oxide in heterostructure, which can have further application in nanoelectronic devices and electrocatalysts.

Dedicated to my family in Taiwan

ACKNOWLEDGMENTS

First, I would like to thank Dr. Qing Hua Wang for willing to take me in to join her group. She helped me a lot and gave me directions in my research. For the times of facing defeat and feeling down, she encouraged me to think positive and recognized the progress that I've done. And most importantly, when things just didn't work out, she helped me to make up my mind in changing the direction and accepted that research is full of uncertainty. I'm thankful for all her patience and guidance in finishing my research.

I also would like to thank my committee member, Dr Alexander Green and Dr. Yu Yao. I'm grateful for them for willing to spend time to help my dissertation and give me advice in experiment and ways to analyze my results. And although Dr. Sefaattin Tongay is not on my committee, I would also like to thank him in granting me access to use his equipment.

Although my research is not all sunshine and roses, but with the help and company from my colleagues the burdens were a little bit more bearable. I'd like to thank Dr. Duo Li in training me using chemical vapor deposition and mechanical exfoliating; Yuqi Guo spent time to help me to familiarize Raman spectroscopy and atomic force microscopy; Suneet Kale shared his experience in MoS_2 single crystal growth and helped calming me down when I'm overwhelmed by anxiety in the last phase of my research; Mahmoud Abed, Matthew Gilliam, and Sanchari Saha helped me with my presentation that really boosted my confidence.

Finally, I'm thankful for my family members. They really supported me in chasing my dreams and even we were separated across the Pacific Ocean with a difference of 13 hours, they still make me feel they are with me all the time.

TABLE OF CONTENTS

Page

CHAPTER Page

LIST OF FIGURES

Figure Page

Figure Page

CHAPTER 1

Introduction and motivation

1.1 Background and Motivation

Two-dimensional (2D) materials are a class of materials that can exist stably in atomically thin sheets. Within the plane, strong covalent bonds hold them together; as for between layers, weak van der Waals (vdW) force take the role to contact layers. In the past 15 years, a surge of researchers has been actively pursuing a vast array of different 2D materials from both fundamental and applied perspectives utilizing this special characteristic of the 2D material to break up their bulk counterpart into free standing flakes. The known types of 2D materials range from graphene[1], an atomically thin sheet of carbon and the most well-known 2D material, and compounds such as the transition metal dichalcogenide (TMDC), hexagonal boron nitride (h-BN), and black phosphorene. The TMDCs are particularly attractive to be used in optical devices[2,3,4] and electronic devices[5,6] due to their promising and tunable electrical, optical and chemical properties[2].

Moreover, to expand the possibility of these materials to meet different application requirements, alterations and combinations of different materials are needed. This thesis demonstrated using air plasma to modify the optical, electronic, and optoelectronic properties of the heterostructure from the combination of MoS_2 and WS_2.

Heterostructure, means integrating two different materials into one structure, is key to transcend the study of 2D material. The combined 2D materials can have synergistic effect that helped to improve or mitigate some drawbacks from using only one material. As in MoS_2 and WS_2, though each of them has good performance in optoelectronic, but when combined into a heterostructure, new functionalities and superior electrical and optoelectronic properties will far exceed the one for their constituents.[7]

Bombarding materials with plasma are a well-established technique for surface modifications, ion doping, and reducing layer thickness for bulk materials. When comes to TMDCs, improvement for stability,[8] carrier mobility[9] and photoresponsivity[10] of TMDC-based devices were documented. In addition to those, from the findings from our group,[11] we documented the change of structure from 2D to 1D. The 1D transition is formed through oxidizing the monolayer TMDC flakes into

transition metal oxide (TMO). This was a significant observation because the facilitate the produce of the rather hard to generate thin film TMO, which usually existed in bulk form due to its covalent bonding between the layers.

Based on these findings, and to the best of our knowledge, no one has done plasma treatment on heterostructure. Hence, it is from our great interest to observe how the surface treatment and the oxidation ability of the air plasma can do to the TMDC heterostructure. The goal will be to find out how can the different TMOs be aligned in a lateral heterostructure setup. And further understand the optoelectronic and electronic properties for possible future applications.

1.2 Structure of the Dissertation

Chapter 1 introduces a brief background on 2D materials and plasma modification processes and provides motivation for applying plasma treatments to 2D materials heterostructures.

Chapter 2 describes more detailed background about TMDC materials, heterostructure, and the plasma treatment mechanisms to set the tone for the most up-to-date developments.

Chapter 3 describes the experimental methods, including sample preparation using chemical vapor deposition (CVD) and micromechanical exfoliation; heterostructure formation using dry transfer for vertical heterostructures and CVD for in-plane heterostructures; and characterization methods like optical microscopy, Raman spectroscopy, and photoluminescence (PL) spectroscopy.

Chapter 4 presents results on optimization of CVD growth conditions to achieve different morphologies and compositions of 2D TMDCs. And further investigate and compare the different optoelectronic responses of the lateral heterostructure in its multi-phases.

Chapter 5 demonstrates O_2 and air plasma treatment on the prepared MoS_2, WS_2, MoS_2/WS_2 heterostructure samples and analyzes the changes in the optical and optoelectronic properties.

Chapter 6 summarizes the work and draws conclusions and presents directions for future research.

CHAPTER 2

BACKGROUND

2.1 Transition Metal Dichalcogenides (TMDCs)

In the established findings of 2D materials, transition metal dichalcogenides (TMDCs) have its spotlight with its intrinsic favorable properties that can provide promising future technology developments. This category of material is often denoted as MX_2, where M stands for transition metals (Mo, W, Nb, In etc.) and X stands for the chalcogen atoms (S, Se, or Te). Structural-wise, the monolayer will be made up of three layers of atoms, which is a layer of transition metals sandwiched by two layers of chalcogen atoms (Fig 2-1 (a)-(b)). From this sandwich structure, they showcased rich possibilities in being from insulators (like HfS_2), semiconductors (like MoS_2), semimetals (WTe_2), and even superconductors ($NbSe_2$). Apart from this versatile property, individually their optical, optoelectronic, and chemical properties also show close relationship with its layer thickness giving them an extra freedom towards application. A good example is MoS_2, which exhibits direct bandgap at 1.8 eV when it is monolayer and shows indirect bandgap at 1.2 eV when bulk, Fig 2-1 (c). Moreover, since the photoluminescence (PL) of the material shared its relationship directly with the bandgap, the PL peak position and intensity as a result will redshift and decline as the layer gets thicker.

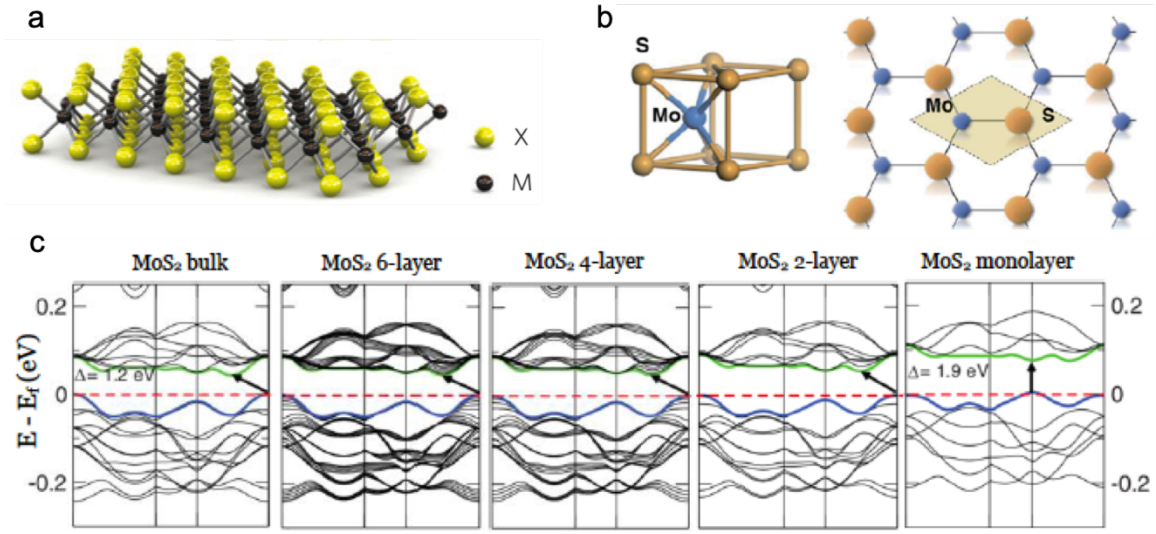

Figure 2-1: TMDCs Properties. (a) typical structure for MX_2 type material. (b) a detailed schematic structure for MoS_2. (c) a bandgap evolution for different thickness of MoS_2, left to right from bulk to monolayer. Figures retrieved from: a, ref. 12; b, ref. 13; c, ref. 14

2.2 Heterostructures

The formation of heterostructure was a difficult task to realize because generally on the connection of dangling bonds need to be fulfilled. This prerequisite as a result produce lattice mismatch which can detriment the property of the structure and makes it challenging to grow good quality heteroepitaxial film, as in Fig 2-2 (a). Luckily, the epitaxial grow of TMDCs follows the other form called the van der Waals (vdW) epitaxy. Under this mechanism, good quality of heterostructure can still be grown even if there are big difference in lattice structure, Fig 2-2 (b).[15]

The heterostructure comes in two general types, vertical heterostructure and lateral heterostructure. The difference is in where and how the interface of the two materials meet and form. For vertical heterostructure, the materials will be stacked layer by layer through weak vdW interaction; while for the lateral heterostructure, the materials will be joined seamlessly in the in-plane fashion, most likely, through covalent bonds. Because vertically stacked heterostructure is easier to achieve, several methods have been developed ranging from micromechanical exfoliation and flake transfer,[16] sequential deposition of 2D material solutions, one-step or multistep CVD growth,[17] and combination of these methods. On the contrast, lateral heterostructure had only CVD growth as the preferred forming mechanism.

When we narrow down to the study of joining two semiconducting materials, from the different location of the conduction band and valence band we can have three different type of band alignments, namely type I, II, and III (Fig 2-2(c)). For MoS_2 and WS_2 heterostructure, it lies in the section of type II, where the lowest conduction band lies in MoS_2 and the highest valence band locates at WS_2. This interesting difference will confine the electrons and holes the separate materials result in excellent performance in optoelectronic device applications like photovoltaic cell.[18]

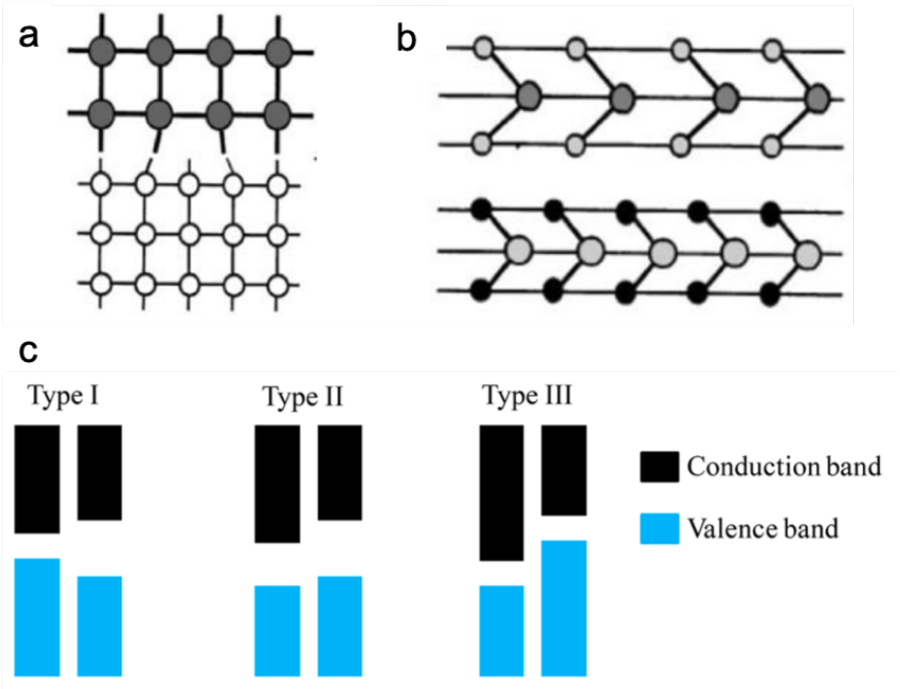

Figure 2-2: Heterostructure Bonding Types and Different Types of Band Alignment. (a)-(b)Interfaces of heterostructures connected by (a) dangling bonds, (b) vdW force. (c) Different type of band alignments from different semiconducting materials. Type I, the minimum of maximum of conduction band and covalent band lies in the same material; type II, the minimum of maximum of conduction band and covalent band lies in different material with no overlap; type III, the minimum of maximum of conduction band and covalent band lies in different material with partial overlap. Figures retrieved from: a-b, ref 15; c, ref 18.

2.3 Plasma modification

Plasma, as one of the fourth fundamental state of matter, is partially ionized gas atoms that composed of electrons, positive and negative ions, excited molecules and radicals generated by electron impact and other reactions. It is a well establish process generally for surface modifications, layer thinning and doping in conventional bulk materials. In 2018, Nan et al organized the most seen application on TMDCs as, reducing layer thickness by etching,[19] n- or p-type, phase transitioning from 2H to 1T, repairing vacancy defect, building heterostructures and self-limiting protective layer formation.[20] But in our group, we documented another reaction of which will change the overall structure of the flake.

Chu et al., found that by treating the free standing MoS_2 and WS_2 with air plasma will not only oxidize the flake but also form transition metal oxides nanoscrolls.[11] Through her effort in trying to deconstruct the steps to find the mechanism by treating the samples with O_2, N_2, N_2/O_2 mixture, and $N_2/O_2/H_2O$ mixture respectively, she found that only $N_2/O_2/H_2O$ mixture will induce nanoscroll formation. After analyzing the possible radicals produced through plasma energizing, the cause of the scrolling reaction is boiled down to three steps. First will be the formation of HNO_3 through the interaction of N2, O2, and H_2O driven by plasma energizing and chemical reaction, showed in (1) and (2).[21-22]

$$3NO_2 + H_2O \longrightarrow 2HNO_3 + NO \quad (1)$$

$$4NO + O_2 + 2H_2O \longrightarrow 4HNO_3 \quad (2)$$

Next, the HNO_3 will then be activated by the plasma as an oxidizing agent to oxidize MoS_2, forming MoO_3, as in (3).[23]

$$MoS_2(s) \xrightarrow{\text{Plasma } HNO_3(g)} MoO_3(s) + SO_2(g) \quad (3)$$

Last, because the oxidization of the top layer of the MoS_2 sandwich structure, lattice distortion and strain were presented from the difference of Mo-S and Mo-O, which were 2.4219 Å and 1.94 Å respectively.[24-25] This in turn will end up generating cracks and forcing the boundary to scroll.

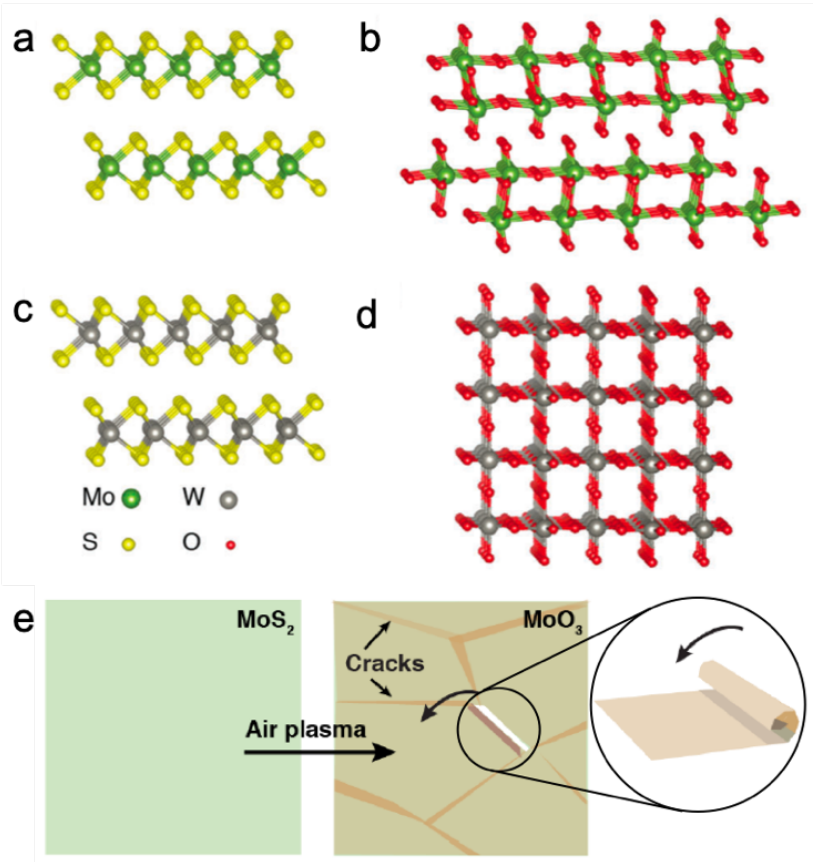

Figure 2-3: Schematic Illustration of Nanoscroll Formation with Air Plasma Treatment. (a)-(d) Crystal structure of MoS_2, MoO_3, WS_2, and WO_3. (e) Evolution of the scrolling mechanism from defect free surface to oxidized surface with cracks and scrolls. Figures retrieved from: a-e, ref 11

CHAPTER 3

CH.3 EXPERIMENTAL METHODS

This project includes several techniques in preparing the samples, namely micromechanical exfoliation, chemical vapor deposition (CVD), dry transfer, and plasma treatment. To characterize the samples, Raman spectroscopy, photoluminescence spectroscopy (PL), and atomic force microscopy (AFM) were used.

3.1 Sample Preparation

3.1.1 Micromechanical Exfoliation

Micromechanical exfoliation, also known as the scotch tape technique, is a way to separate bulk materials into thinner layers through repeated peeling using adhesive tape. Large domains of graphene, single layer MoS_2, and single layer WS_2 were obtained by this method and transferred onto SiO_2 (300 nm)/Si substrates (Wafernet, Inc.). The silicon wafer with tape and layered crystals were placed onto a hotplate preheated to 120ºC (actual measured temperature 80ºC) for 1.5 minute before peeling, which greatly helped to obtain larger monolayer crystals with a cleaner substrate with much less tape residue. Finally, to remove the tape residue, water, and adsorbed gas, the transferred sample was annealed at 300ºC for 3 hours in a dedicated quartz tube pumped down to around 38 mtorr with 200 sccm of Ar flowing through.

3.1.2 Single-Crystal Chemical Vapor Deposition

Atmospheric pressure chemical vapor deposition (APCVD) was used to grow single-crystals of MoS_2, and WS_2. The target substrates were SiO_2/Si wafers cut into dimensions of 1.8 cm x 4 cm. The wafers were sonicated in the sequence of acetone and isopropyl alcohol for 5 minutes each and blown dry with N_2. Meanwhile, the plasma cleaner (Harrick Plasma, model PDC-32G, and gas flow controller Plasmaflo PDC-FMG) was first pre-cleaned by pumping down to 80 mtorr then introducing with O_2 to about 800 mtorr for a 5-minute cycle with a high RF level setting (18W power). Next, the washed sample was cleaned in the plasma chamber after pumping down to ~80 mtorr, filled with O_2 to ~800 mtorr, and at high power for 10 minutes.

MoS_2 Growth

For the MoS_2 single-crystal, the growth was executed with a two-zone system with only Ar flowing through. The heating zones was separated into two parts. First, the high heating zone was a hot-wall tube furnace (ThermoFisher Lindberg/Blue M). Second, the low heating zone will be wrapped with a heating tape (BriskHeat Silicone Rubber Heating Tapes (BS0) 4ft. long 120V) connected to a variac (EX ELECTRONIX EXPRESS Variable Transformer, 300 VAC Max, 0-130V Output, 3 Amp) to adjust the power. The solid S powder precursor (80 mg, Alfa Aesar, 99.5%) was loaded on another SiO_2/Si substrate (1.8 cm by 1.8 cm) and placed into a 1″ diameter quartz tube located upstream at the low heating zone. The middle of the S was placed 32 cm away from the center of the high heat zone. The other precursor was MoO_3 powder precursor (20 mg, Sigma-Aldrich, 99%) which was loaded on another SiO_2/Si substrate (1.8 cm by 0.4 cm) and placed into a quartz boat in the center of the high heat zone furnace downstream. The target wafer was placed with SiO_2 facing down toward MoO_3. To begin, the quartz tube was first purged with Ar at 200 sccm for 10 minutes then turned down to 10 sccm before heating. Next, the high heat zone was heated to 500ºC in 12 minutes to get rid of moisture in the tube then to 720ºC in 20 minute and stayed for 5 minutes. On the other hand, the low heat zone was raised to 150ºC when high heat zone reached growth temperature. At shut down, the heating tape was turned off right after the growth session, but the furnace lid remained closed for gradual cooling to 570ºC (about 20 minutes) then followed with quenching with the lid opened exposing to ambient air.

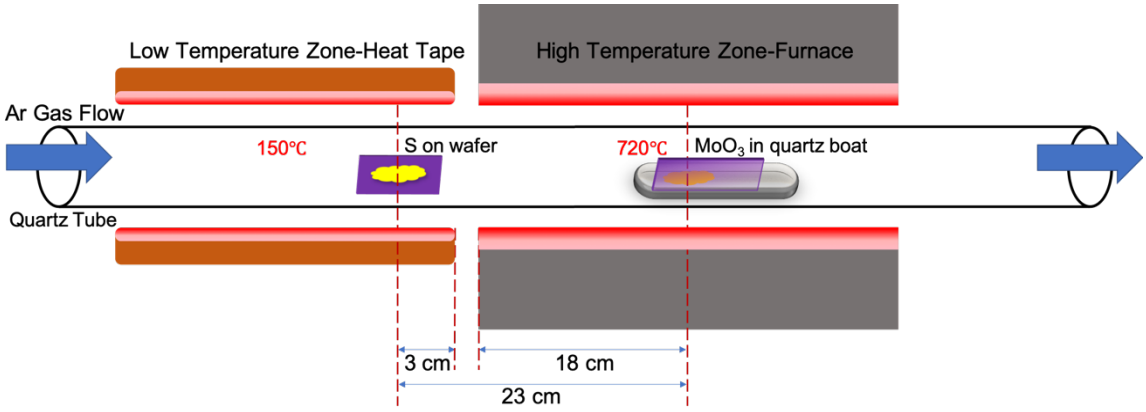

Figure 3-1 Schematic Illustration of CVD Setup for the MoS_2.

WS_2 Growth

For the WS_2 single-crystal, the growth was also done with the two heating zone setup like MoS_2, but the carrier gas was a mixture of Ar and H_2 .[26] The amount of S used in WS_2 growth was also 80 mg and placed at the same upstream position of the 1″ diameter quartz tube attached with low heating zone. The other precursor was $WO_{2.9}$ (70 mg, Alfa Aesar, 99.99%) instead of the commonly used WO_3, because of its higher yield according to Liu et al.[27] Crushed NaCl (30mg, Alfa Aesar, ≥ 99.5%) was also added to the $WO_{2.9}$ as a growth promoter according to Li et al.[17] T The $WO_{2.9}$ and NaCl was well mixed with a spatula then put into a ceramic boat instead of quartz boat because molten NaCl will corrode quartz boat. Next, the middle of the boat was placed downstream in the high heat zone 33 cm away from the middle of the S with cleaned wafer SiO_2 side facing down overlaid on top. To start, the quartz tube was purged with 500 sccm of Ar for 10 minutes, then turned down to 80 sccm to begin the growth cycle. The high heat zone was first heated to 500ºC in 20 minutes to get rid of moisture then ramped up to 825ºC in 30 minutes and last stayed for 5 minutes. The low heat zone was heated to 150ºC when high heat zone reached growth temperature. Lastly, the shutdown was done in the same way as MoS_2.

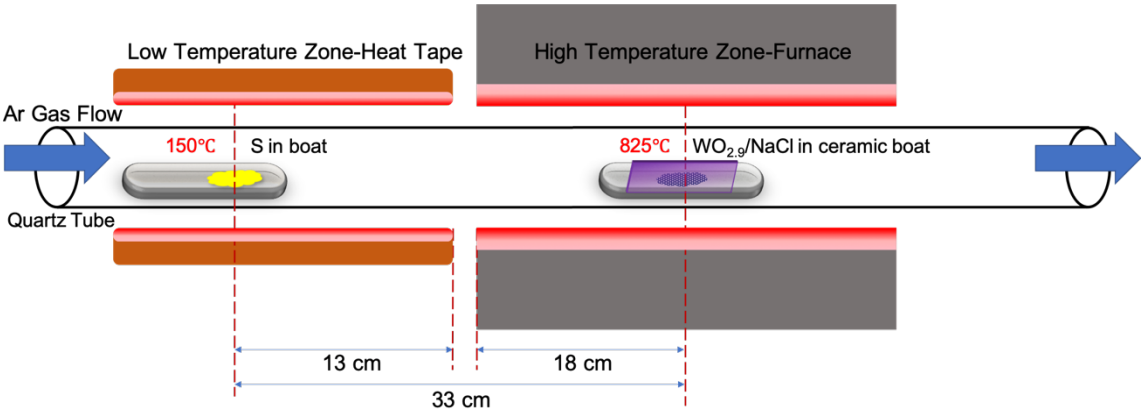

Figure 3-2: Schematic Illustration of CVD Setup for the WS_2.

3.1.3 TMDC Heterostructure Formation

For the MoS_2/WS_2 heterostructure, both top-down and bottom-up approaches were used. The top-down method was the dry transfer technique [28] to transfer the as-grown MoS_2 onto WS_2 flake to form a vertical stacked heterostructure. The bottom-up method was the one-stage CVD epitaxial growth method to form a lateral in-plane heterostructure.[29]

Top-down: Dry Transfer

The dry transfer technique uses a long working distance microscope to help precisely position the flake, Fig 3-3. First, to prepare the stamp, the selected part of the MoS_2/SiO_2 substrate is covered with freshly cut PDMS. Then the PDMS/MoS_2/SiO_2 structure is floated onto a bath of 2M KOH at 80ºC for around 5 min to etch away the SiO_2, resulting only in PDMS/MoS_2 left floating. Next, it is rinsed with DI water, blown dry with N_2 gas, and placed onto a clean glass slab that will be fastened to a XYZ direction table with the MoS_2 side facing down. Second, to form the heterostructure, the microscope is adjusted to switch between different view planes to align the target WS_2 substrate and the MoS_2 flake. The stamp is then lowered to overlap the two flakes. As the two layers touch, the color changes indicating the transition and adhesion. Lastly, the stamp is lifted off slowly to leave the heterostructure intact. The governing mechanism in this technique is the viscoelastic response of the elastomer stamp. Because of the viscoelasticity phenomenon, in a short time frame the elastomer stamp acts as a rigid solid and in a longer time frame the elastomer acts more like liquid, so when peeling the stamp off slowly the affinity between the stamp and flake is weaker than the van der Waals force between the two layered materials in the heterostructure.[30]

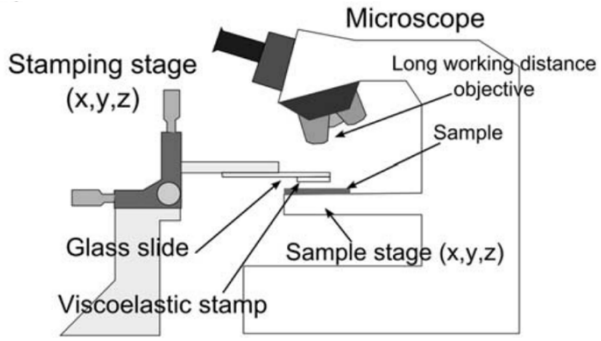

Figure 3-3: Schematic Illustration of the Dry Transfer Setup. Figures retrieved from: ref 30

Top-down: CVD One Step Growth

For the CVD growth of heterostructures, the preparation for the substrate is same as the single-crystal growth as mentioned. Also, throughout the whole growth, only 80 sccm of Ar as used as the carrier gas. The difference is in with the precursors: at the high heat zone the ceramic boat contains in sequence of 30 μg of NaCl, 14.2 mg mixture of $WO_{2.9}$ (10 mg) and NaCl (4.2 mg), and 5 mg of MoO_3; at the low heat zone, the quartz boat contains 10 mg of S.[29] The temperature curve of the high heating zone was the same as the WS_2 growing curve but the S in the low heating zone was heated to 200℃ to provide higher concentration of S vapor.

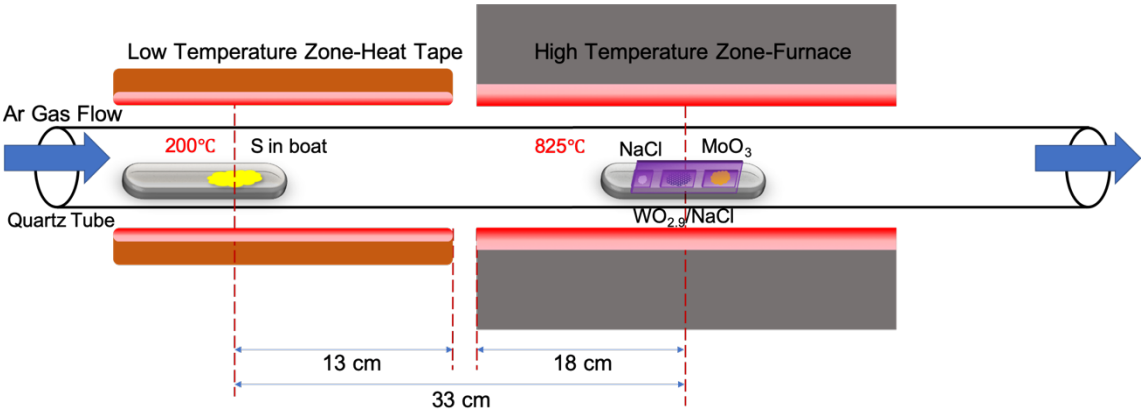

Figure 3-4: Schematic Illustration of CVD Setup for the MoS_2/WS_2 Heterostructure.

3.2 Plasma Treatment

The as-exfoliated and as-grown CVD samples was put into the plasma cleaner that had gone through cleaning cycle and pumped to around 80 mTorr vacuum. Next, ambient lab air (relative humidity 60%, at 18°C) was introduced into the chamber reaching approximately 800 torr through gas inlet valve for 5 minutes to perform the air plasma treatment. The plasma was turned on for 2 to 4 seconds at 18 W, high power mode.

3.3 Optical Characterization

3.3.1 Raman and Photoluminescence Spectroscopy

Raman and photoluminescence (PL) measurements were used to characterize the thickness of the TMDC layers and the integrity of the structure, respectively. The samples were characterized

using WITec alpha300R confocal Raman microscope system with a 532 nm excitation laser and 100X objective lens that can achieve ~1μm laser spot size. The intensity of the laser power was controlled to be less than 0.32 mW to protect the TMDC thin film from being damaged. When acquiring single spectrum, the integration time and accumulation were 5 s with 2 times averaging; for mapping, it was 0.5 s with 1 time for each spot. The gratings for Raman and PL spectra were 1800 and 300 grooves/mm, respectively.

3.3.2 Atomic Force Microscopy

Atomic force microscopy (AFM) was performed in ScanAsyst noncontact mode on a Bruker Multimode V system with ScanAsyst-Air tips (Bruker). The Gwyddion software package[31] was used to process the image and obtain the height profile.

CHAPTER 4

SYNTHESIS OF 2D MATERIALS AND HETEROSTRUCTURES

This project can be divided into two main parts. The first part is establishing the optimal growth parameters to obtain single crystals of transition metal dichalcogenides (TMDCs), namely MoS_2 and WS_2 and forming MoS_2/WS_2 heterostructures. The second part is focused on making nanoscrolls from the monolayers and heterostructures using the plasma surface modification process.

4.1 Synthesis of 2D Materials and Heterostructures

CVD is the growth technique of forming atomic thin layer single-crystals. Vaporized precursors are carried downstream using a carrier gas into the reacting zone in a tube furnace to mingle and condense to the chosen substrate. Utilizing CVD to grow samples requires an understanding of how each possible parameter will steer the resulting deposited materials. These parameters include the pressure, temperature, distance, growth time, cleanness of substrate, precursor chemicals, and carrier gas. In this project, due to time limitations, some parameters were based on literature values that reports of large dimension flakes (>50 μm), while a couple of other parameters were investigated.

4.1.1 Pressure

For growing MoS_2, low-pressure chemical vapor deposition (LPCVD) was first tried, but it only resulted in uniform but polycrystalline MoS_2 with very small domains that were not suitable for nanoscroll formation. The growth conditions that were used were ~1.63 torr working pressure with 300 sccm flow of Ar. Thus, atmospheric pressure chemical vapor deposition (APCVD) was implemented to grow large single crystals of MoS_2. The pivotal reason that allows APCVD to achieve bigger single crystal than LPCVD is because of the difference in the mean free path (λ) of the gas molecules as well as the molecules condensed on the substrate.

$$\lambda = \frac{kT}{\sqrt{2}\pi d^2 P}$$

where

$$z = \sqrt{2}\pi d^2 \bar{v} \frac{P}{kT}$$

and k is the Boltzmann constant, P is the pressure, T is the temperature, and z is the collision frequency of the molecule. As the pressure in the quartz tube increases (to 760 torr), z also increases, resulting in a higher reaction rate and a higher nucleation rate by promoting the chemical reaction between precursors or between precursor clusters and substrate. [32]

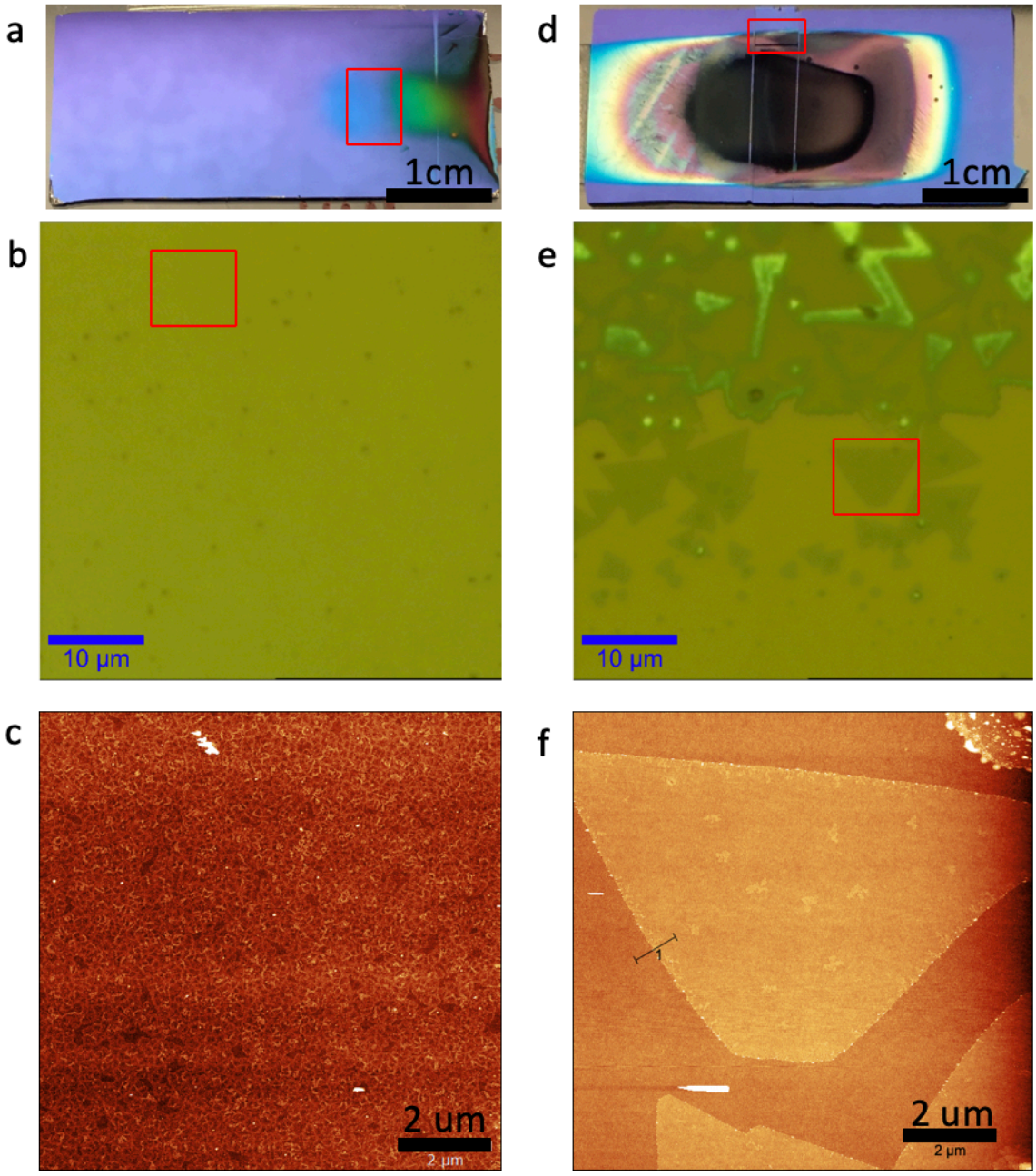

Figure 4-1: LPCVD and APCVD. (a) As-grown LCVD substrate (b) Optical microscopy image of the single-crystal MoS_2 from LPCVD. (c) AFM image of the uniform coverage. (d)-(e) Substrate, optical and AFM image of APCVD outcome where MoS_2 single-crystal is highlighted.

4.1.2 Temperature Ramp Rate

During the times when one furnace setup was used, if the parameters were all the same except the temperature gradient, it showed that when ramping from 150ºC to 850ºC, MoS_2 tend to grow the best at 70℃/min with the biggest single crystal coverage.

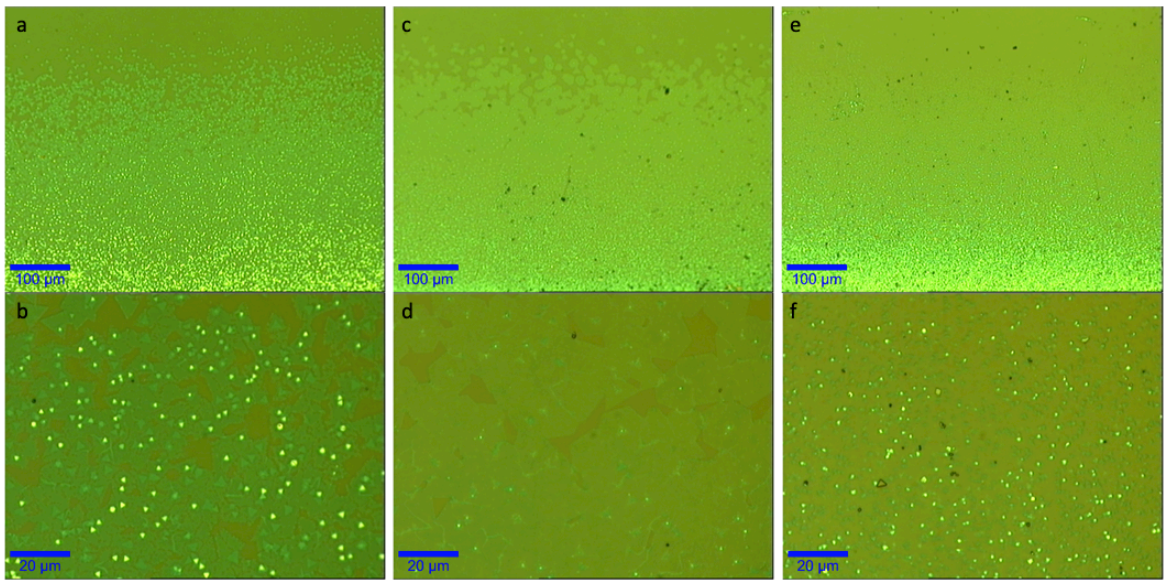

Figure 4-2: APCVD Outcome in Different Temperature Ramp Rate. (a)-(b) At 50ºC/min. (c)-(d) At 70ºC/min. (e)-(f) At 100ºC/min.

4.1.3 $WO_{2.9}$ and Halide assisted Growth

At the beginning of this project, the growth of WS_2, because of the high melting point of WO_3, at 1473 °C,was the most challenging because it was very challenging to get any formations on the substrate. Most of the early attempts left most of the precursors intact. After encountering respectively to the study from van der Vlies et al. and Li at al., the breakthrough needed finally arrived. [17],[33]

First was about using $WO_{2.9}$ instead of WO_3; it was found that because of the high W–O bond energy, it is hard to directly sulfurize W^{6+} if no other intermediates are formed. To incorporate S into the WO_3 lattice, reduction of W^{6+} to W5+ is essential. Luckily, $WO_{2.9}$ have been partially reduced to W^{5+} or W^{4+} ions so it favors the transition. [33]

Second, by mixing NaCl with $WO_{2.9}$ as the precursor, instead of direct sulfurizing $WO_{2.9}$, an alternative reaction is proposed to take place:

$$WO_{2.9}(s) + NaCl(s) \rightarrow NaWO_3(s) + WOCl_4(g) + WO_2Cl_2(g) + WO_2(s) + W(s)$$

$$WOCl_4(g) + WO_2Cl_2(g) + S(g) + H_2(g) \rightarrow WS_2(s) + HCl(g) + H_2O(g)$$

The melting point of WO_2Cl_2 ($\boxed{T_m^{WO_2Cl_2}}$ = 265 ◦C) and $WOCl_4$ ($\boxed{T_m^{WOCl_4}}$ = 211 ◦C), which are way lower than the WO_3 and as a result facilitating the growth.[34] Moreover, the reaction using this precursor can be documented back from 2008.[35]

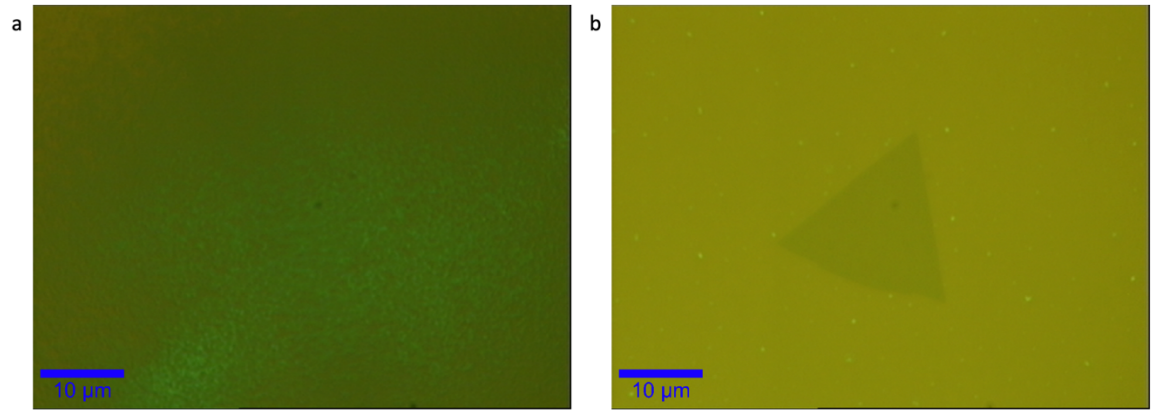

Figure 4-3: Different CVD Outcomes from Different Precursors. (a)WO_3 and (b)$WO_{2.9}$ with NaCl mixture

4.2 Results from Chemical Vapor Deposition

4.2.1 MoS_2 Single-Crystal

Optical Microscopy Characterization

From the as-grown substrate, a different gradient of color indicates the different thickness of the MoS_2 deposit, from the thickest part in black to the thinnest portion in blue. The contrast purple color in the surrounding will be the bare SiO_2 substrate. Typically, triangular single-crystal MoS_2 can be found in the edges of the blue area, an example will be where the red box in Fig4-4(a) indicates. Throughout all the documented samples, the largest MoS_2 single-crystal is ~10um with an example of Fig4-4(b). As for the more uniform regions and the transition region are Fig4-4(c) and Fig4-4(d) respectively.

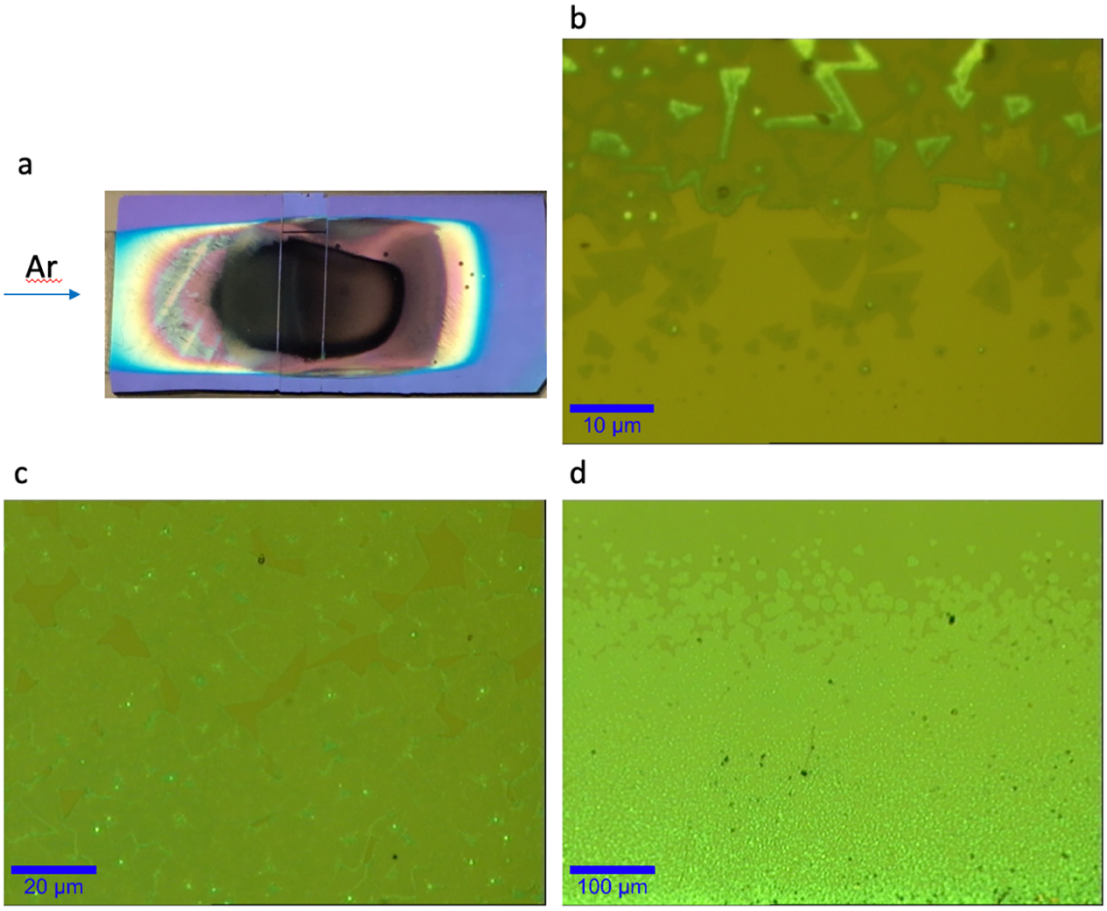

Figure 4-4: Typical MoS_2 CVD Growth (a)As-grown substrate (b)-(d) 100X, 50X, and 10X optical lens outcome.

Raman Spectroscopy

To confirm the layer thickness of the thin film and flake of the sample, Raman spectroscopy is employed. There are two signature Raman shift peaks for the triangular flake in Fig 4-5(a) at around at 383.3 cm^{-1} and 404 cm^{-1}, which is out-of-plane (A_{1g}) and in-plane (E^1_{2g}) vibrations of S and Mo atoms respectively. The difference(Δ) value of them is 20.7 cm^{-1}, proving that the flake is a single layer MoS_2.[36] In addition, bulk area of the MoS_2 growth is also characterized and found that the difference of the Raman shift is enlarged to 27.6 cm^{-1}, with the A_{1g} redshift to 408.6 cm^{-1} and E^1_{2g} blueshift to 381 cm-1. Moreover, to confirm the uniformity of the chosen flake, mapping was also conducted showing in Fig4-5(b). From any given point on the triangle of the mapping, A_{1g} and E^1_{2g} both stick to around 383 and 404 cm^{-1} which further assured that the growth was desirable.

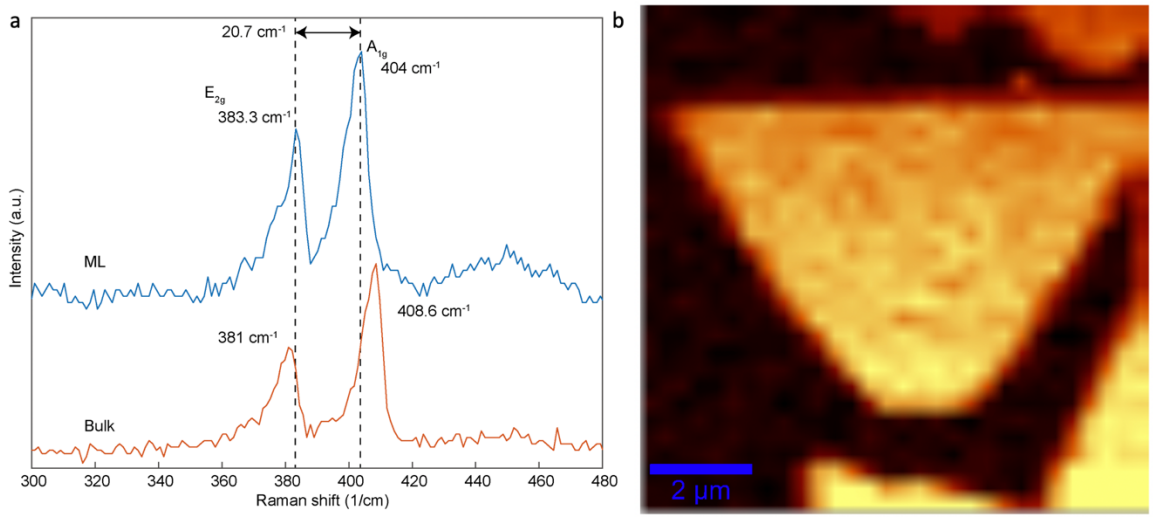

Figure 4-5: Raman Spectroscopy of Monolayer and Bulk MoS_2. (a)Monolayer Raman shift with out-of-plane vibration peak (E_{2g}) at 383.3 cm^{-1} and in-plane vibration peak (A_{1g}) at 404 cm^{-1}, making the difference of the peak (Δ) around 20.7 cm^{-1}; whereas for bulk MoS_2 the difference is enlarged into 27.6 cm^{-1} (b)Raman mapping of monolayer (from 380 to 420 cm^{-1})

Photoluminescence Spectroscopy (PL)

Addition to Raman shift, PL peaks also serve as a good indicator for characterizing the layer thickness of the MoS_2 outcome. It is because the thickness of the layer will influence the intensity and location of the peak. In Fig4-6(a), the blue line which indicates the monolayer MoS_2, two peaks at 1.845 eV and 1.98 eV were observed, which refer to A1 and B1 excitons.[37,38] The A excitonic emission is assigned to the direct transition from the conduction band minimum to the uppermost valence band maximum at the K valley in the Brillouin zone; as for the B exciton, corresponding to the direct transition from the conduction band minimum to the lower valence band maximum at the K valleys. A simplified band diagram is shown in the Fig4-6(c) [39,40]

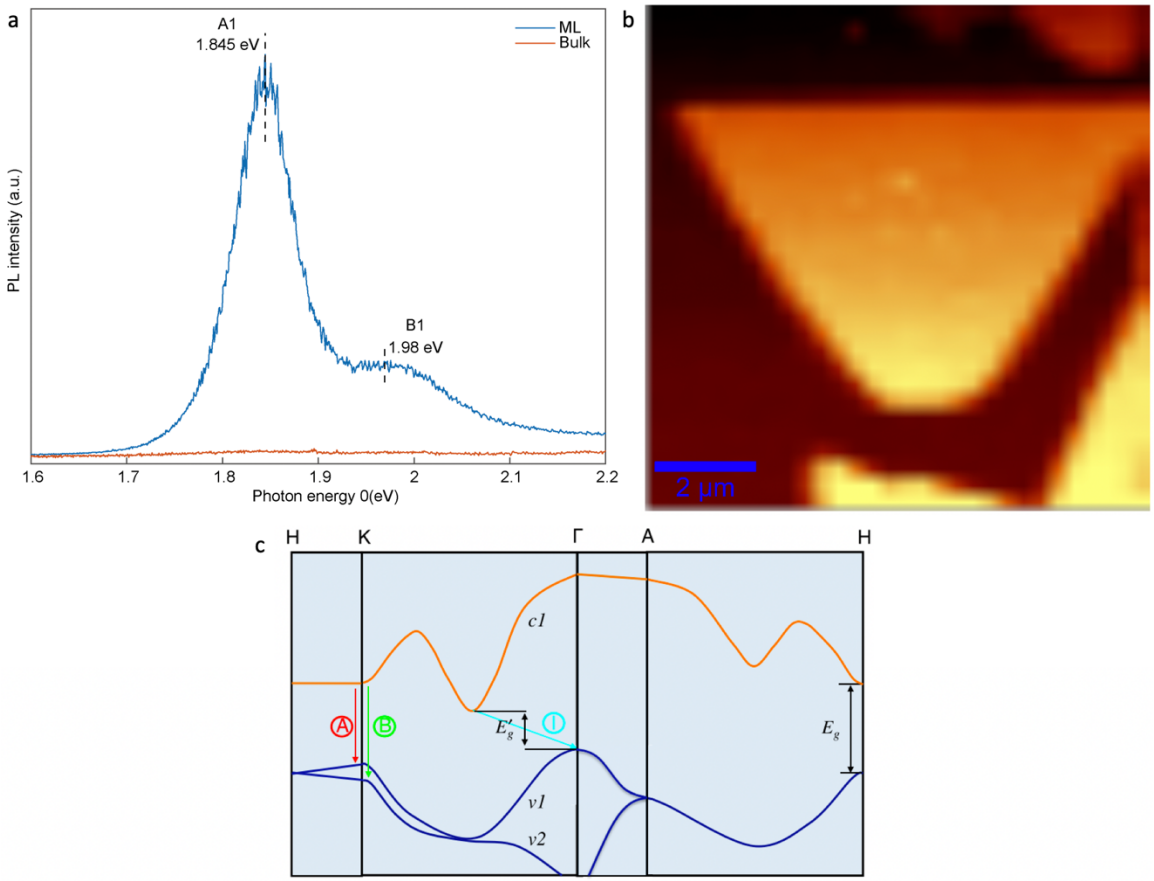

Figure 4-6: Photoluminescence of Monolayer and Bulk MoS_2. (a) The blue line indicates the monolayer MoS_2 PL peak with A1 exciton at 1.845 eV and B1 exciton at 1.98eV; Orange line indicates the bulk MoS_2 PL. (b) PL Mapping of the monolayer MoS_2 (from 1.7 to 2.08 eV) (c) An simplified band structure of bulk MoS_2, showing the lowest conduction band c1 and the highest split valence bands v1 and v2. A and B are the direct-gap transitions, and I is the indirect-gap transition. E'_g is the indirect gap for the bulk, and E_g is the direct gap for the monolayer. Figures retrieved from: e, ref 39

Atomic force microscopy (AFM)

To further understand the physical thickness of the monolayer, AFM was utilized to understand its topology. In Fig4-7(a)-(b), the crystal growth of the MoS_2 with a clean cut on the edges and a rather smooth surface manifests that it is a single-crystal growth with the thickness of 0.8nm. On the contrary, at the other spot on the substrate, which is Fig 4-7(c)-(d), it is readily seen to be a merge of two crystal with a grain boundary in white curving in the middle and with the top grain stacking another layer of MoS_2.

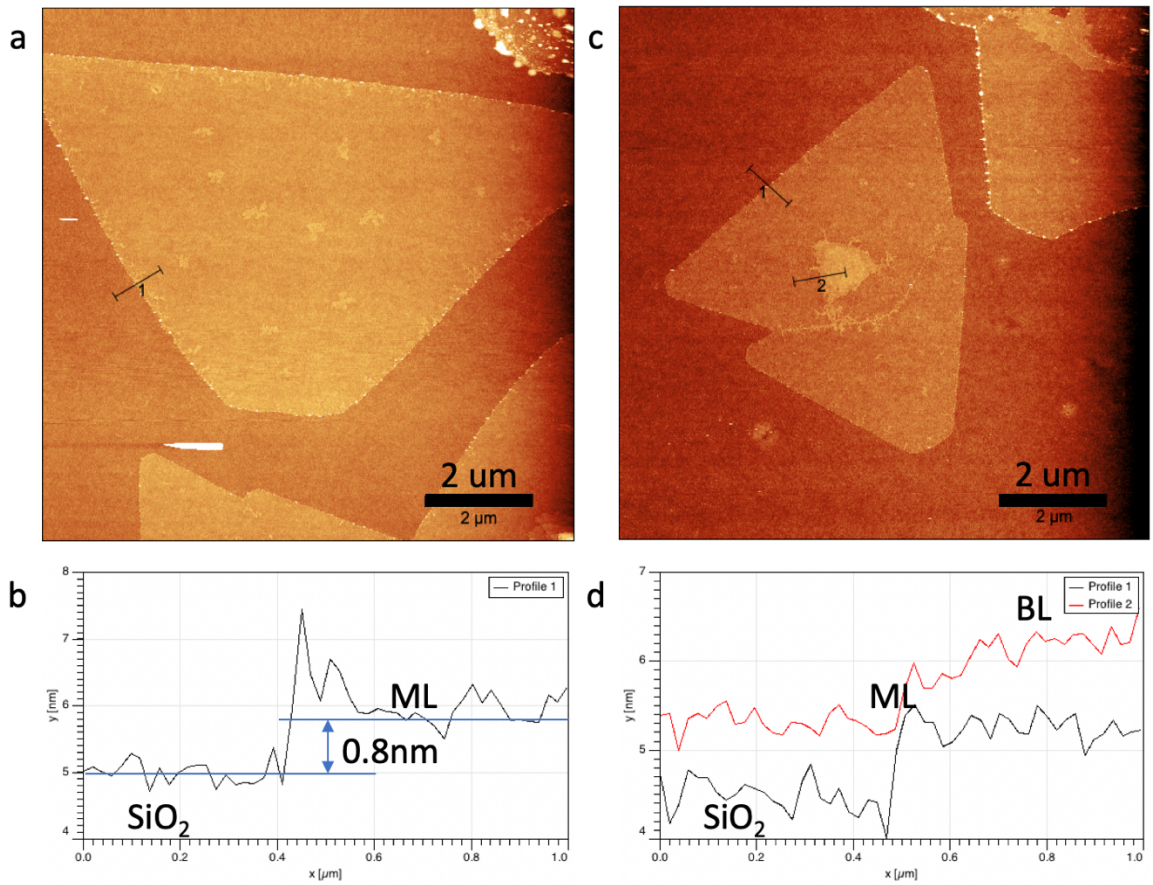

Figure 4-7: Atomic Force Microscopy of Different MoS_2 Outcome. (a)-(b) single-crystal monolayer MoS_2 and (c)-(d) a merge of two MoS_2 crystal grain with the top one growing a second layer

4.2.2 WS_2 Single-Crystal

Optical Microscopy Characterization

For a typical WS_2 CVD growth outcome, the substrate will be shown in Fig 4-8 (a)-(b). The single crystals in the flake is distributed throughout the substrate without a long-range uniform layer

formation, unlike the one seen in MoS_2 growth. For the largest documented flake for the growth will be around 40 to 50 μm in size. And it was observed that using this technique uniform layers of WS_2 is not likely to form. As for using one-step heterostructure CVD growth, at the upstream part where only WS_2 was forming, mm size thick WS_2 single crystal can be seen on the bare substrate in Fig 4-8(c). And in Fig 4-8(d), an example of a single crystal with domain size around 300 μm is presented.

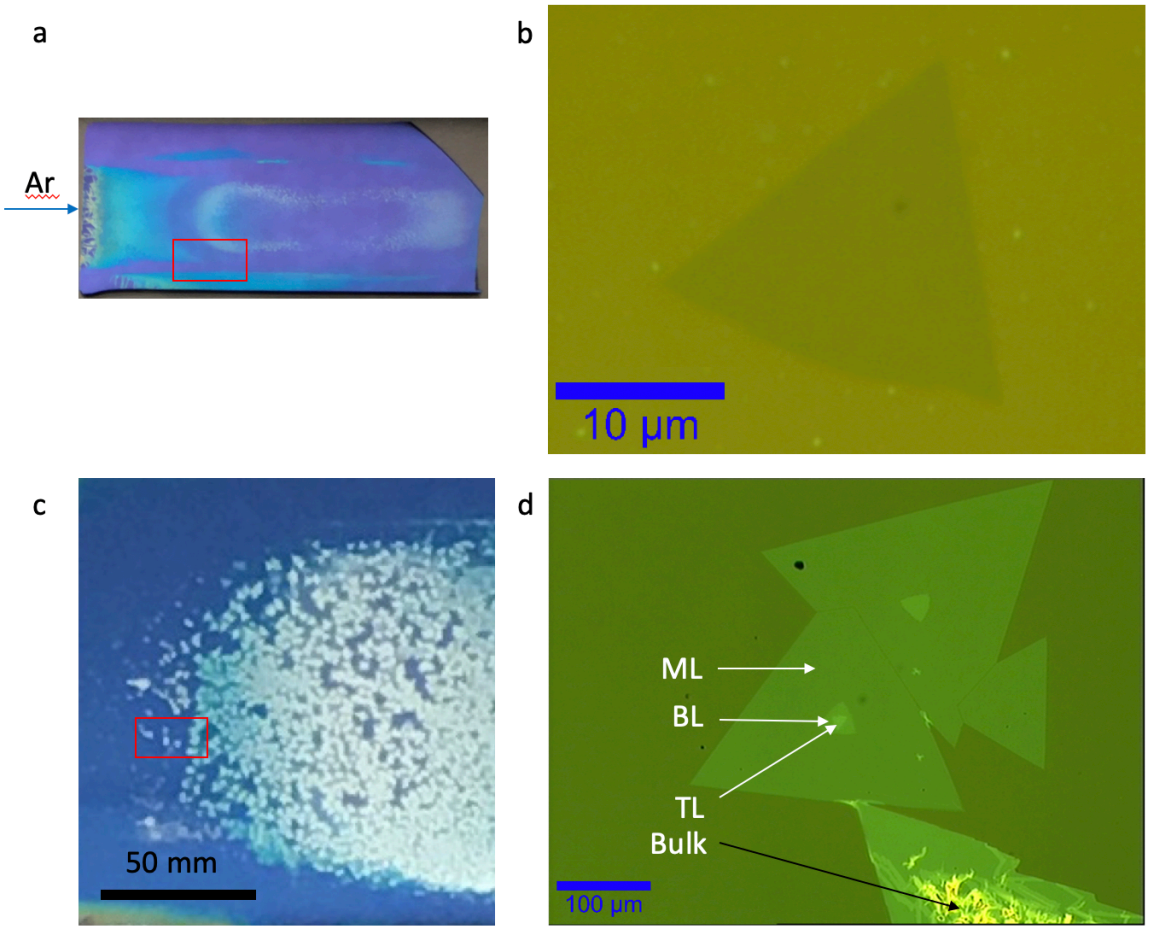

Figure 4-8: Optical Characterization of WS_2 CVD Growth. (a)-(b) Typical WS_2 CVD growth and (c)-(d) the upper WS_2 part of the one step heterostructure growth

Raman Spectroscopy

In Fig 4-9(b), two prominent peaks can be found at 348.6 cm-1 and 418.6 cm-1, which are attributed to the merge of both 2LA (longitudinal acoustic) and out-of-plane vibration (E^1_{2g}) and in-plane vibration (A_{1g}) of W-S respectively.[41,42] The difference of them will be 70 cm-1, which agreed to other paper to showcase to be monolayer. Moreover, for WS_2, the peak intensity ratio (I_{2LA}/I_{A1g})

of the 2LA to A_{1g} is also highly sensitive to its thickness. From the result the in Fig 4-9(b)and(d), for monolayers (ML), the $I_{2LA}/I_{A1g} \geq 5$; for bilayer (BL), the $I_{2LA}/I_{A1g} \leq 5$; for bulk, the $I_{2LA}/I_{A1g}=1$.

From the mapping of the uniform monolayer in Fig 4-9(a), it can clearly be seen that the middle of the flake is much more uniform than the outer rim. The analysis will be further discussed in detail in next session. And in Fig 4-9(c), the mapping shows that as the layer grows the intensity of the peak will drop in general, leaving the ML to be the brightest and TL to be the darkest.

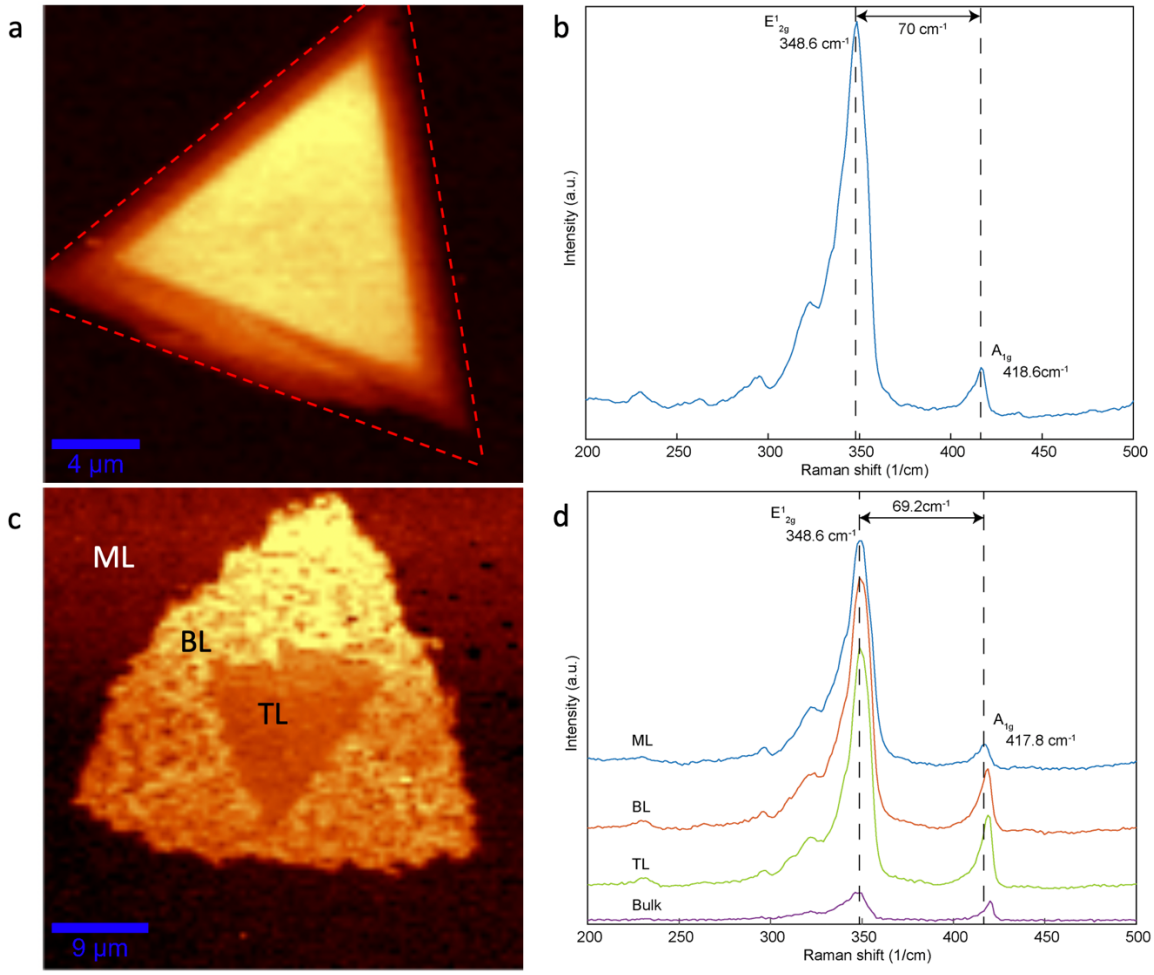

Figure 4-9 Raman Mapping and Single Spectrum of WS_2. (a)-(b) Mapping with dotted line indicating the single crystal area and (b) single spectrum of monolayer WS_2. (c)-(d)Mapping and single spectrum of monolayer, bilayer, and trilayer. Where a clear redshift can be seen in A_{1g}.

Photoluminescence Spectroscopy (PL)

The PL peaks are directly related to the bandgap of the WS_2 structure, which for a monolayer of WS_2 at the K point in the Brillouin zones a direct transition can be seen in Fig 4-10(e). These transitions are calculated to be at A (1.95 eV), wherefrom the result in Fig 4-10(b) and (d), the big spike will be very close to it at 1.956eV and 1.961 eV respectively further proving the result to be monolayer. And in Fig 4-10(d) where the spectrum of different layers was taken, as the layer got thicker a trend of decrease of energy or redshift and broaden the width can be observed.

As mentioned in the MoS_2, PL mapping can be used to in characterizing the overall structure outcome, because if there is any defect, the result will not be uniform. But from the outcome in Fig 4-10(a), the overall mapping shows rather good uniformity and suggests that the growth outcome is in good crystallinity with small defects. This is different from other reported literature that have resulted in brighter edges and almost dark in the middle part of the crystal. To optimize and understand this phenomenon, Peimyoo et al had found that changing the way the sulfur was introduced into the system will vary the result. If the sulfur used one furnace growth technique, placing it near the furnace inlet without another heat source, the WS_2 outcome will be highly doped by S resulting in distortions and weakening of PL intensity. However, if the S is introduced from afar with an extra heat source, like the setup in this work, the growth is freer of doping and hence resulting in a relatively uniform PL intensity.[43]

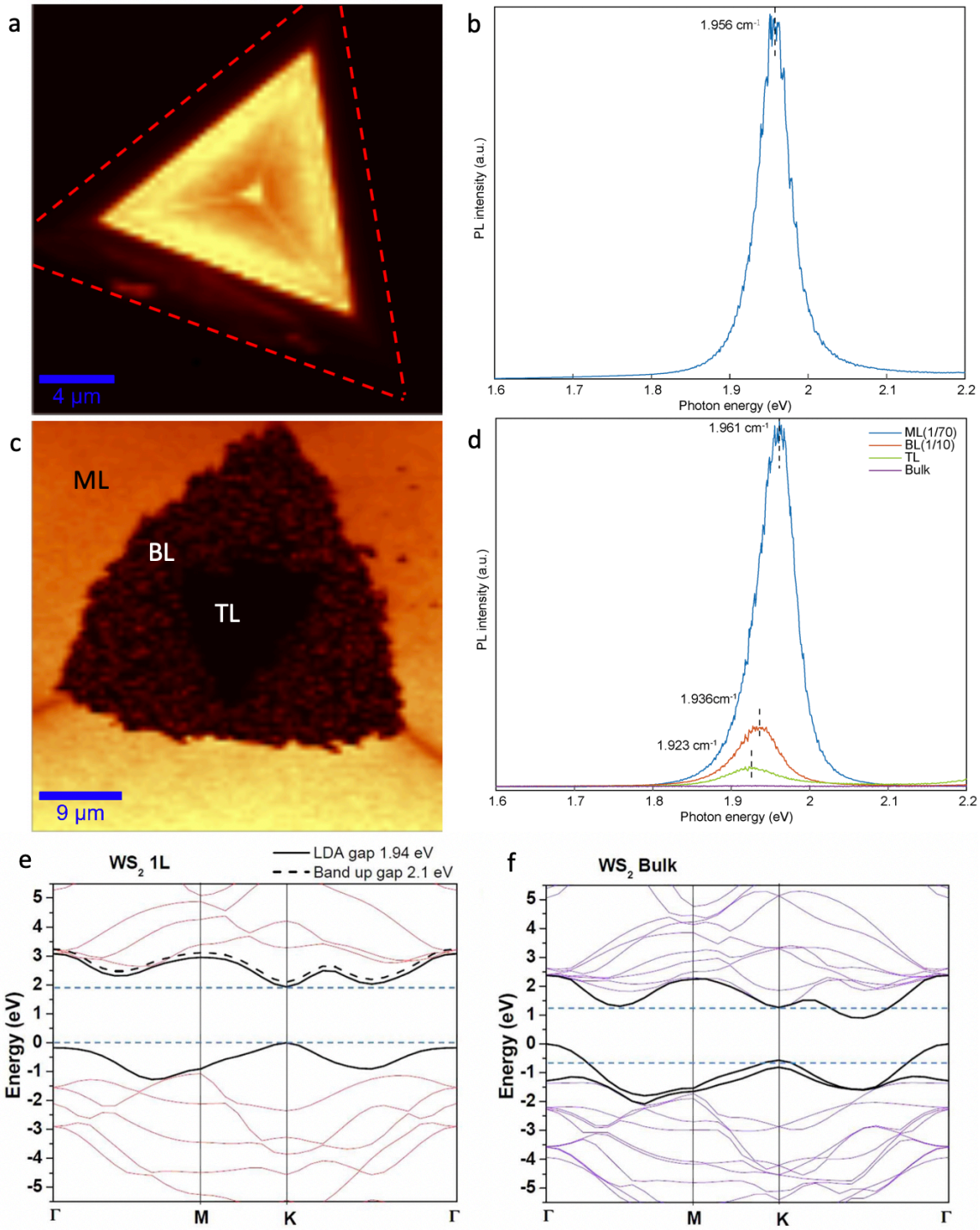

Figure 4-10 PL Mapping, Single Spectrum and DFT Calculated Band Structure of WS_2. (a) Mapping (from 1.7 to 2.08 eV) with dotted line indicating the single crystal area and (b) single spectrum of monolayer WS_2. (c)-(d) Mapping and a single spectrum of monolayer, bilayer, and trilayer. (e)-(f) band structure of monolayer and bulk WS_2, where direct bandgap can be seen in ML at 1.94 eV and indirect bandgap is found in bulk form. Figures retrieved from: e-f, ref 41

Atomic Force Microscopy (AFM)

To determine the height of the monolayer and the morphology of the monolayer single-crystal flake, AFM was utilized. From Fig 4-11(b), about 0.8nm is the height of the as-grown WS_2 flake, which was similar to the other reported findings.[42,44] It is worthy to mention that in Fig 4-11(a) the background of the SiO_2 substrate is full of wrinkles which is not be able to see with optical, Raman, and PL characterization. By judging from the growth procedure and the possible chemical reactions, it was proposed that NaOH might be produced during the reaction and reacted with the SiO_2 surface leaving these textures on the surface.

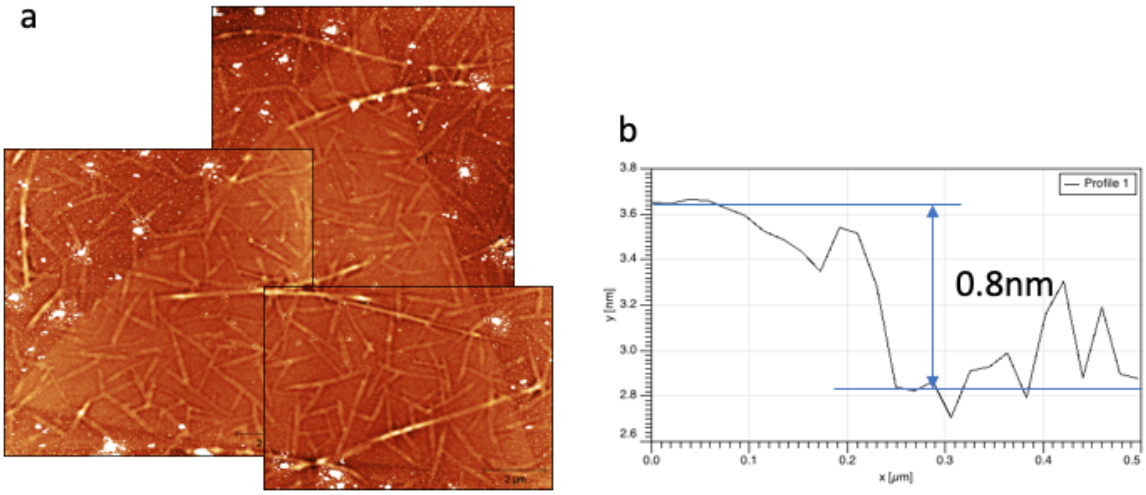

Figure 4-11: AFM Image of Monolayer Single-Crystal WS_2. (a) AFM image merged from three images (b) the height of the flake showing 0.8nm

Optoelectronic Properties Mapping Analysis

From the optoelectronic mapping outcome of Raman shift and PL, different intensity response from the crystal shows decay and segmentation of the crystal. In general, the areas are split into two parts, the *core* where a clear bright triangular shape can be observed and the dimming *rim* spanning out. To further characterize the result, cross section of the intensity mapping and the single spectrum in different areas were taken to show more detail.

In Raman mapping, the cross section showed a plateau in the core indicating that the overall uniformity of the crystal structure in this area; on the contrary, in the rim the decay is prominent showing that the WS_2 at this part of crystal the crystallinity decays. It can be attribute to the lack of time for the precursor to from in the end to cooling session of the growth.

From the PL mapping, the bright core area was segmented into three equal areas with the boundary from the vertices to the center of the triangle. And within each domain, the intensity is highest in the center and the edge. The cross section of the mapping in Fig 4-12 (d) further clarified this trend. The quench of the PL response can be explained in different ways, namely defects, strain, and doping. The most straightforward theory will be the defects located in the semiconductors, such as mid-gap states at the boundaries, which facilities non-radiative recombination. The almost dark outer rim should be the direct result from this cause because of the loose structure indicated by the Raman spectrum. Next, because Raman frequencies, which are strain-sensitive, are uniform across the entire bright core area, hence we rule out inhomogeneous strain as a possible cause for the inhomogeneous exciton energy. Last, the doping or the anomalies can also be highly influential, but without the technique of elemental characterization like EDS to see how the constituent of the specific area was formed; as well as structural characterization like TEM to see the structure arrangement, it is hard to judge at this point.

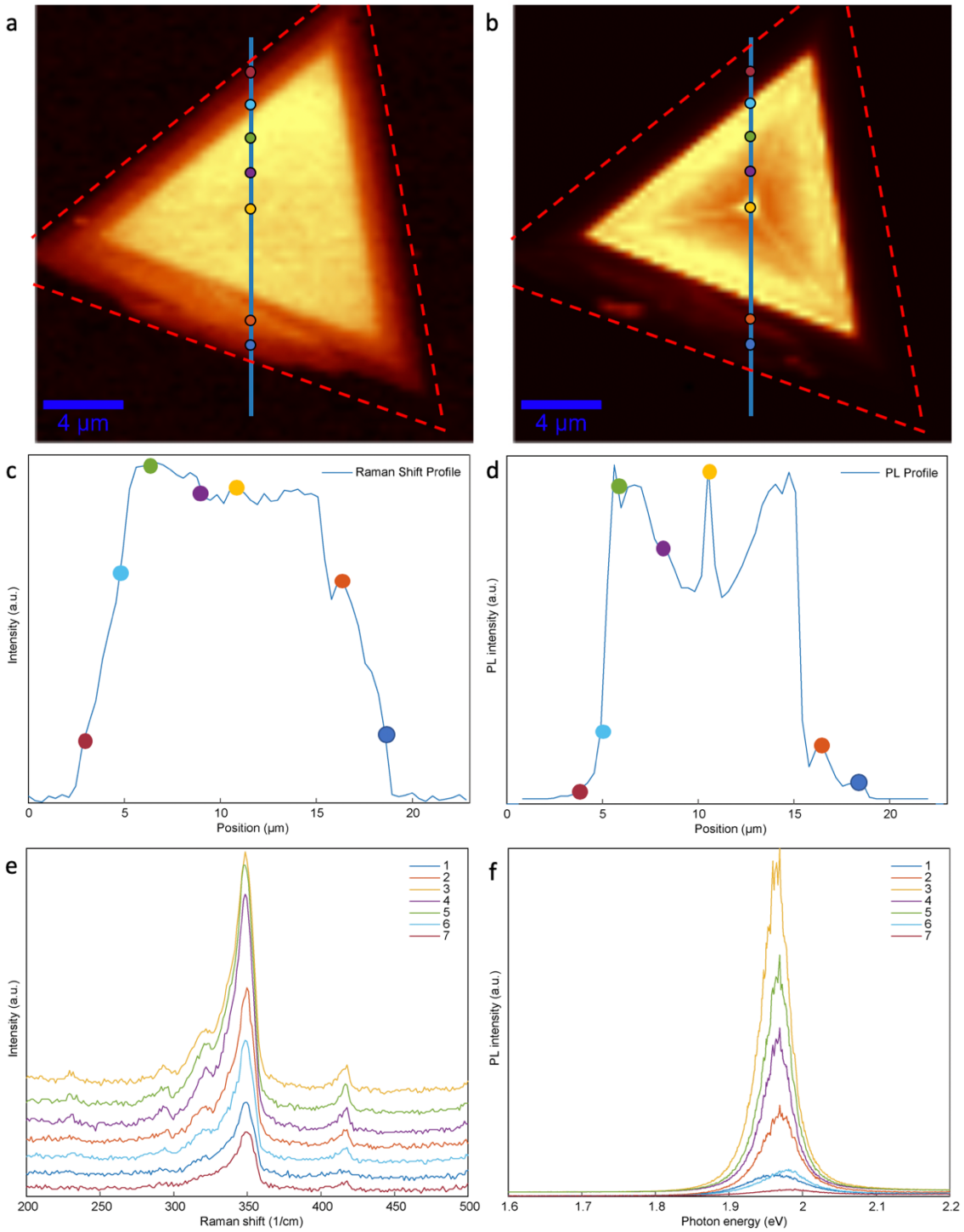

Figure 4-12 Raman and PL Mapping Analysis. (a)-(b) Raman and PL mapping with a blue line indicating location of (c)-(d) the intensity cross section profile and (e)-(f) dots showing the place where the single spectrum was taking.

4.2.3 MoS_2/WS_2 Heterostructure

Top-down - Dry Transfer

To obtain heterostructure, transferring the well-established single-crystal MoS_2 and WS_2 through dry transfer was the most effective and efficient way. By using this deterministic method, it is easier to position the flake to observe desired outcome, no matter to have them totally overlap or partially overlap. However, after a few attempts, there two issues came. First, as shown in Fig 4-12(a)-(b), wrinkles can be seen in the overlapping MoS_2 flake, which will affect the overall PL outcome. As observed in Fig 4-12(c)-(d), which are Raman mapping of MoS_2 and WS_2 respectively, the overall outcome of the flake is uniform. However, when scanned for PL in Fig 4-12(e), the mapping shows that there is different intensity on the surface, proving the assumption. Second, since the angle cannot be freely adjusted, lattice mismatch will come in as an influential factor.

Despite the drawbacks, in Fig 4-12(f)-(g), the Raman shift and PL single spectrum of heterostructure did show the combination but quenched peaks of MoS_2 and WS_2 as expected. In the Raman shift, the freestanding MoS_2 peaks are at 385.6 cm^{-1} and 405.1 cm^{-1}; WS_2 peaks are at 349.8 cm^{-1} and 417.8 cm^{-1}; heterostructure peaks will be at 349.8 cm^{-1}, 383.3 cm^{-1}, 404 cm^{-1}, and 417.8 cm^{-1}. It is expected as the MoS_2 was placed on top of the WS_2 crystal which will affect the Mo-S interaction. For PL, the exhibited peaks for the heterostructure are positioned at 1.85 eV and 2.0 eV, consistent with what was found for MoS_2 (1.86 eV) and WS_2(1.98 eV). The noticeable weaker of the PL intensity is due to the interlayer relaxation of excitons. Because the difference and mismatch of band structure between the heterostructure layer, they formed a type II semiconductor, meaning that the photoexcited charges between the two layers will be separated. This separation ends up with electrons to MoS_2 film and holes to WS_2 film (Fig 4-12(g) inset), which decreases the spatial overlap between the wave functions of electrons and holes, subsequently leading to the decrease in PL efficiency.[45] It can also be seen in Fig 4-12(e), where the part of MoS_2 that wasn't overlapped with WS_2 showing slight brighter response than the overlapped part.

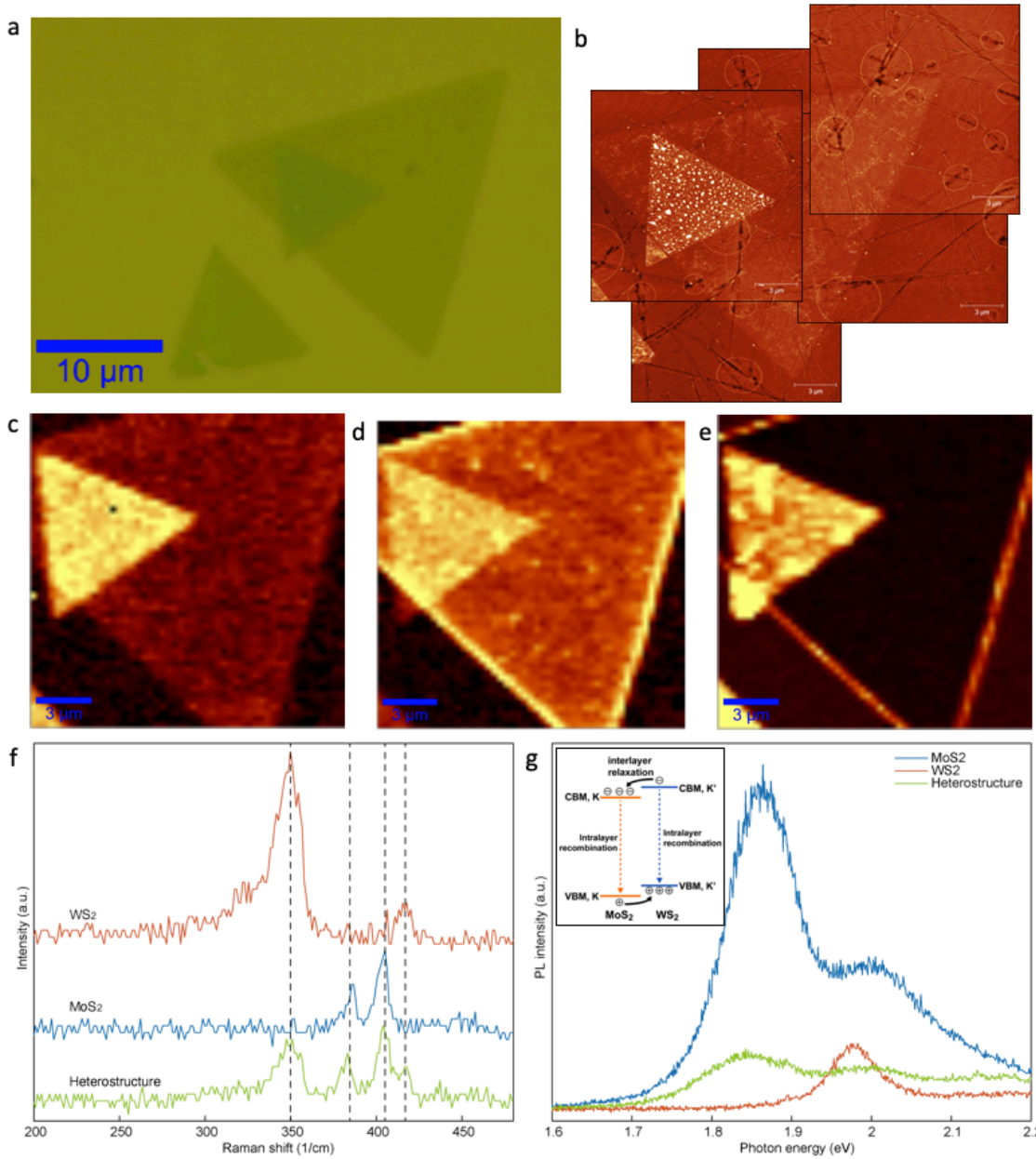

Figure 4-13: Dry Transfer Outcome of MoS_2/WS_2 Heterostructure. (a) The optical spectrum of MoS_2 on top of WS_2 after transfer. (b) AFM showing transfer wrinkles in white dot from MoS_2. (c) MoS_2 Raman mapping showing uniform response (380-420 cm^{-1}). (d) WS_2 Raman mapping showing a part of the MoS_2 because of the overlap of wavelength. The response is uniform throughout the flake with the edge higher in intensity (300 to 425 cm^{-1}). (e) PL mapping of the heterostructure (1.7 to 2.08 eV). (f)-(g) Single spectrum of Raman shift and PL at the different spot of the heterostructure. The inset chart showing the interlayer relaxation of the exciton. Figures retrieved from: g inset chart, ref 45

Bottom-Up - One Step CVD of Heterostructure

To manufacture the heterostructure that is comparably free of lattice mismatch and defect, one step of CVD growth is a crucial method to develop. In the as-grown substrate, Fig 4-13(a), different forms of crystals are documented, including single-crystals of MoS_2, WS_2, and $Mo_xW_{1-x}S_2$. Among these formations, heterostructure of the single crystals in vertical and lateral fashion can also be observed. Position wise, the left upstream part only forms WS_2 single-crystal and the downstream right part will form a mixture of heterostructure and MoS_2 single-crystal. The middle is where the most heterostructure was found, for both vertical and lateral heterostructure, Fig 4-13 (b)-(c). From the Raman mapping in Fig 4-13(d) and (f), the middle bright spot is where MoS_2 formed and WS_2 condensed along the boundary. Moreover, through the PL mapping in Fig 4-13 (e) and (g), the uniformity of the intensity further assured the integrity of the crystal structure.

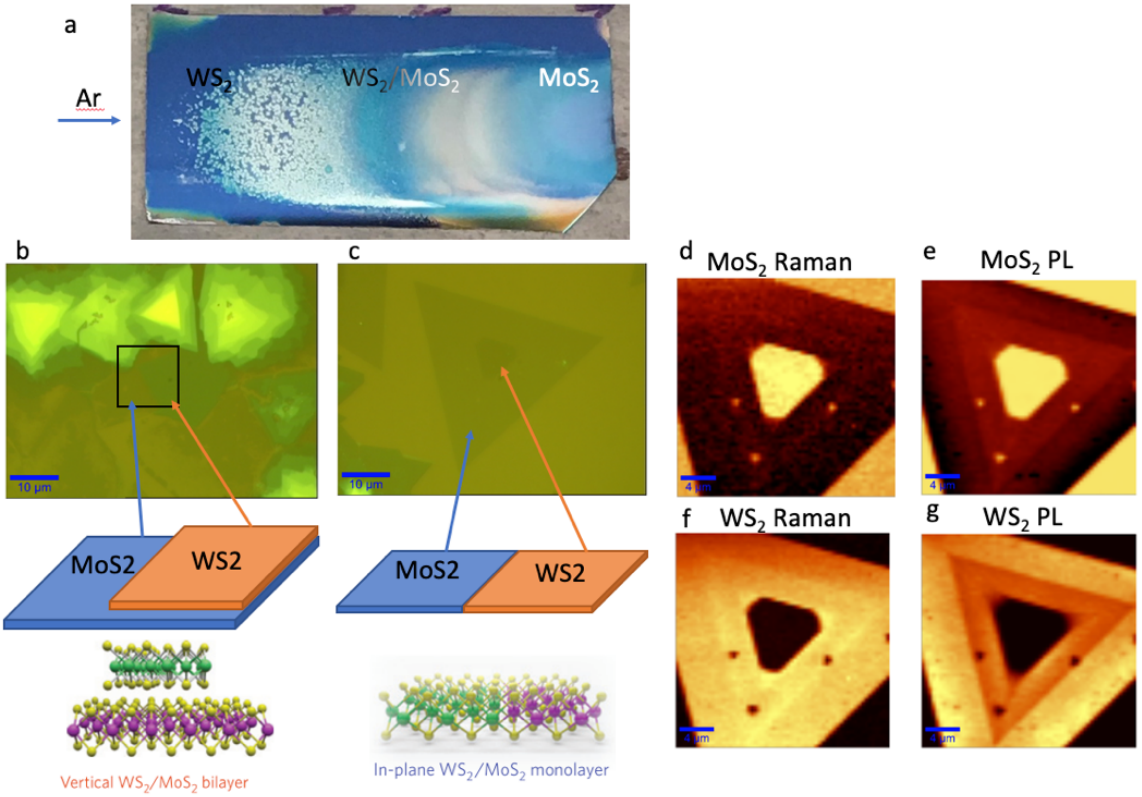

Figure 4-14: Vertical and Lateral Heterostructures from WS_2/MoS_2 Monolayers. (a) The as-grown substrate with WS_2, WS_2/MoS_2, and MoS_2 forming from left to right. (b)-(c) A typical vertical and lateral heterostructure with the schematic showcase with blocks and molecular simulation. (d)-(e) Raman and PL mapping of MoS_2 for lateral heterostructure. (f)-(g) Raman and PL mapping of WS_2 for lateral heterostructure. Figures retrieved from: b-c inset 3D structure, ref 46

Lateral Heterostructure Phase Analysis

Though the mapping, prominent PL segmentation can be observed. With detailed analysis of the Raman shift and PL spectrum, the segmentation was found to be the result of different combination of the W, Mo, and S constituents. After confirming with other report,[29] the center was MoS_2, the peaks of the core were WS_2/MoS_2 heterostructures, the first rim was the $W_{1-x}Mo_xS_2$ alloy, and then the last rim was WS_2, Fig 4-12 (a)-(b). These multiple phases gave us insight of the different response of the structures. From the Raman shift response, Fig 4-14 (c), the peaks for WS_2, MoS_2, and the heterostructure were just as what we have documented with distinctive 2 and 4 signature peaks respectively. But for the $W_{1-x}Mo_xS_2$ alloy we observed a three peaks response made up of a weak peak at 296 cm^{-1} and two WS_2 signature peaks. As for PL response, Fig 4-12 (d), we found that the intensity being highest in WS_2 outer rim decaying to the lowest in MoS_2 core.

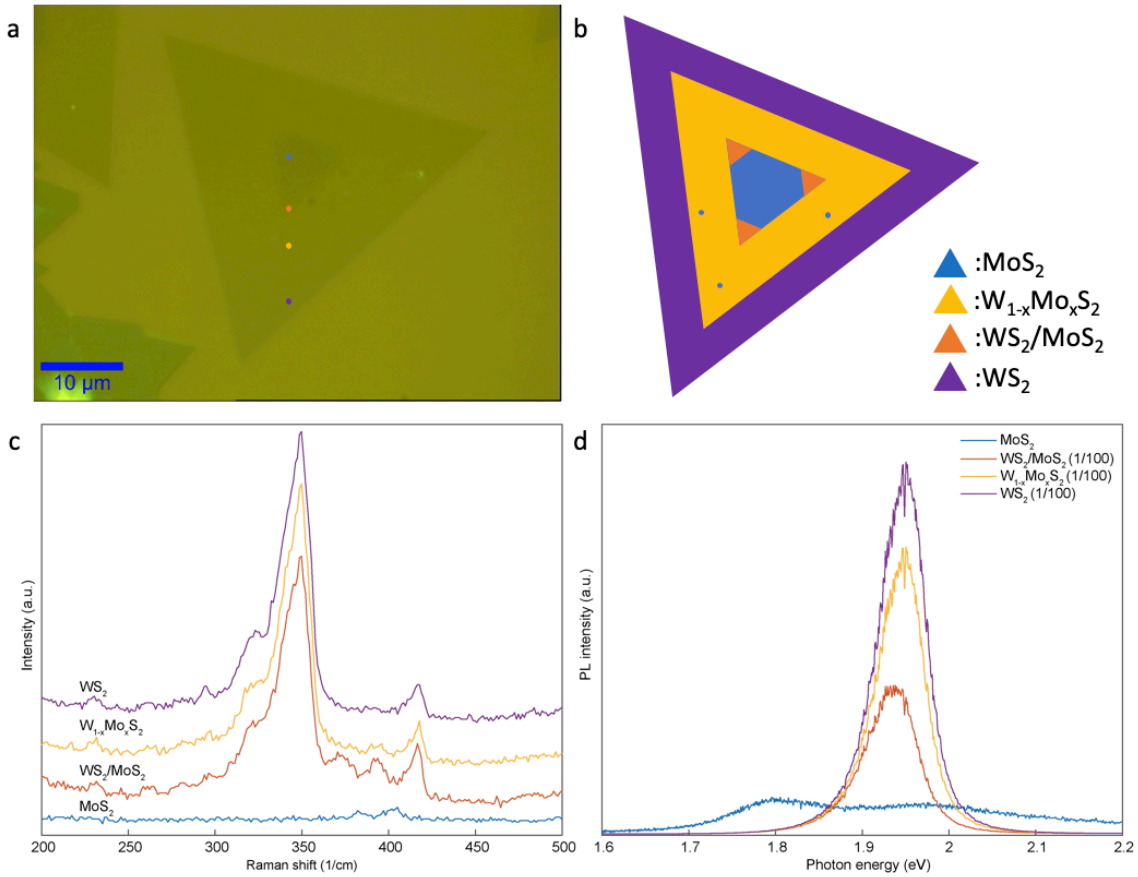

Figure 4-15: Lateral Heterostructure Mapping Analysis. (a) Optical image decorated with colored dots indicating the position of the single spectrum. (b) Schematic illustration of the different phases of lateral heterostructure. (c)-(d) Raman and PL single spectrum.

CHAPTER 5

PLASMA TREATMENT

In this project, to investigate how air and oxygen plasma can physically and chemically modify the morphology and optoelectronic performance of the heterostructure, few stages were designed. First was the observations of how air and oxygen plasma process effect on monolayer of MoS_2 and WS_2 flakes. Next stage was how these plasmas influenced with vertical and lateral TMDC heterostructures. This air plasma technique was first proposed by Chu et al., using the high energy of air plasma to introduce defects and cause oxidization. She observed scrolling and cracks with the monolayer MoS_2 and WS_2.[11]

5.1 Oxygen plasma

5.1.1 MoS_2

From the optical characterization, Fig.5-1(a) and (c), the monolayer MoS_2 flake didn't show a big difference. Whereas through the Raman and PL single spectrum, Fig 5-1 (e) and (f), the intensities of the post treatment are lower than the pristine flake and the width (FWHM) of the peaks were broaden. Moreover, for Raman shift, the A_{1g} and E^1_{2g} peak was blue shifted by 1 cm^{-1} and 5cm^{-1} respectively. Follow with the disappearing of the LAM mode at 450 cm^{-1} also suggested the disruption of the MoS_2 lattice during the oxygen plasma treatment. [47] Lastly, from the AFM outcome, which are Fig 4-13 (b) and (d), not only there is an increase of height of the overall flake from 0.9 nm to 1.5 nm, cracks are formed. This suggest that the distortion of the lattice result might be a result of the expansion of the structure.

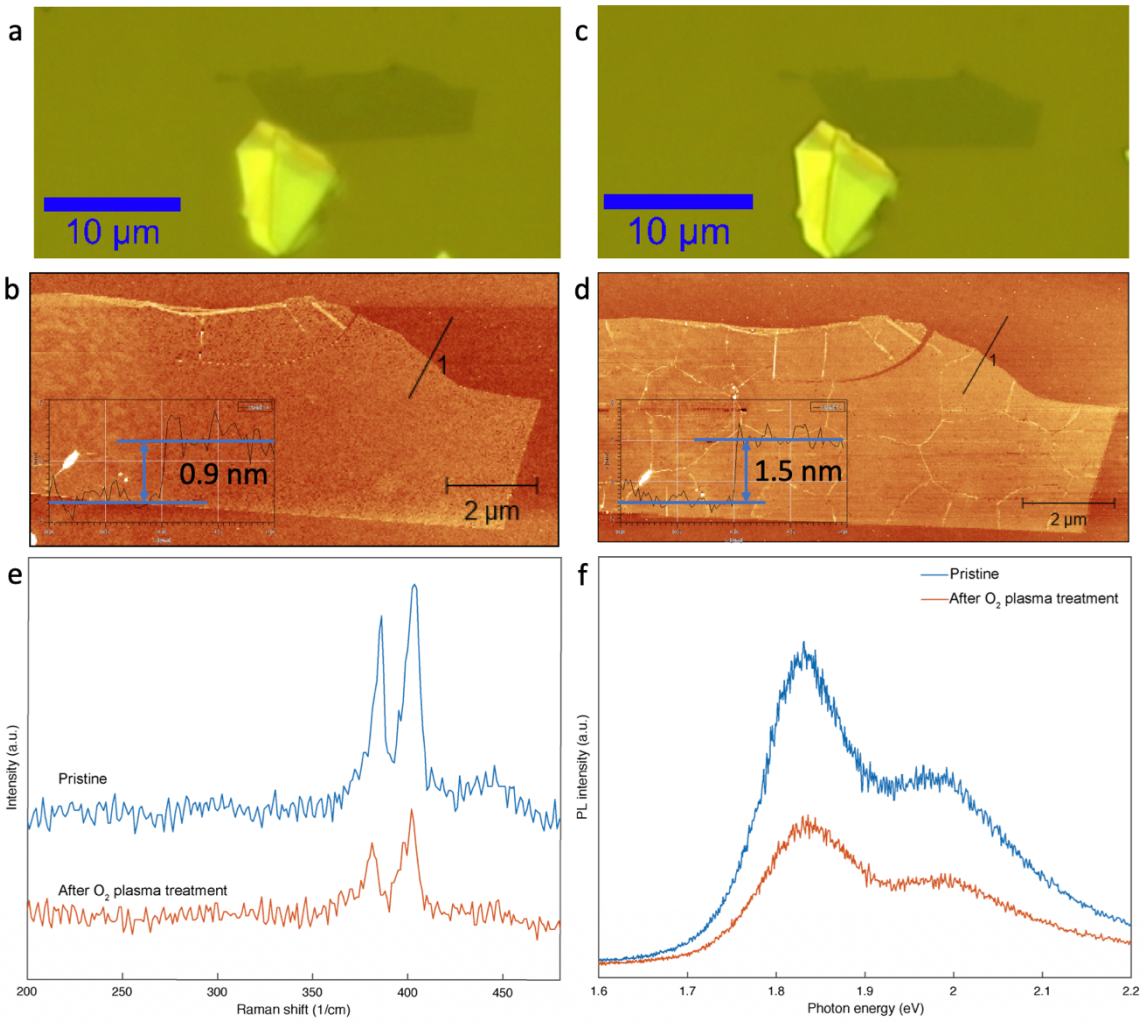

Figure 5-1: Mechanically Exfoliated Monolayer MoS_2 2s O_2 Plasma Treatment. (a)&(c) Optical image of before and after the treatment. (b)&(d) AFM image of before and after treatment, showing an increase of flake thickness with the inset profile. (e)-(f) The single spectrum of Raman shift and PL response, both indicating that the treatment decreased the intensities.

5.1.2 WS_2

As for WS_2, from the result, it was surprising that for both Raman shift and PL, the peak intensities from after behaves better than before the process. Judging from the AFM scanning outcome, the reason of how this happened might be because after the O_2 plasma treatment, the covered tape residue was etched away by the plasma, leaving the flake a smoother surface and more uniform structure. Hence the intensity of the Raman shift and PL become higher.

In addition to smoothing the surface, when compared to the post treatment of MoS_2, where the flake was thickened homogeneously throughout the plane, the thickening of WS_2 were slightly higher at the rim. This finding showed us that the deformation of WS_2 is either easier on the edges or in general the thickening of the flake starts form the edges.

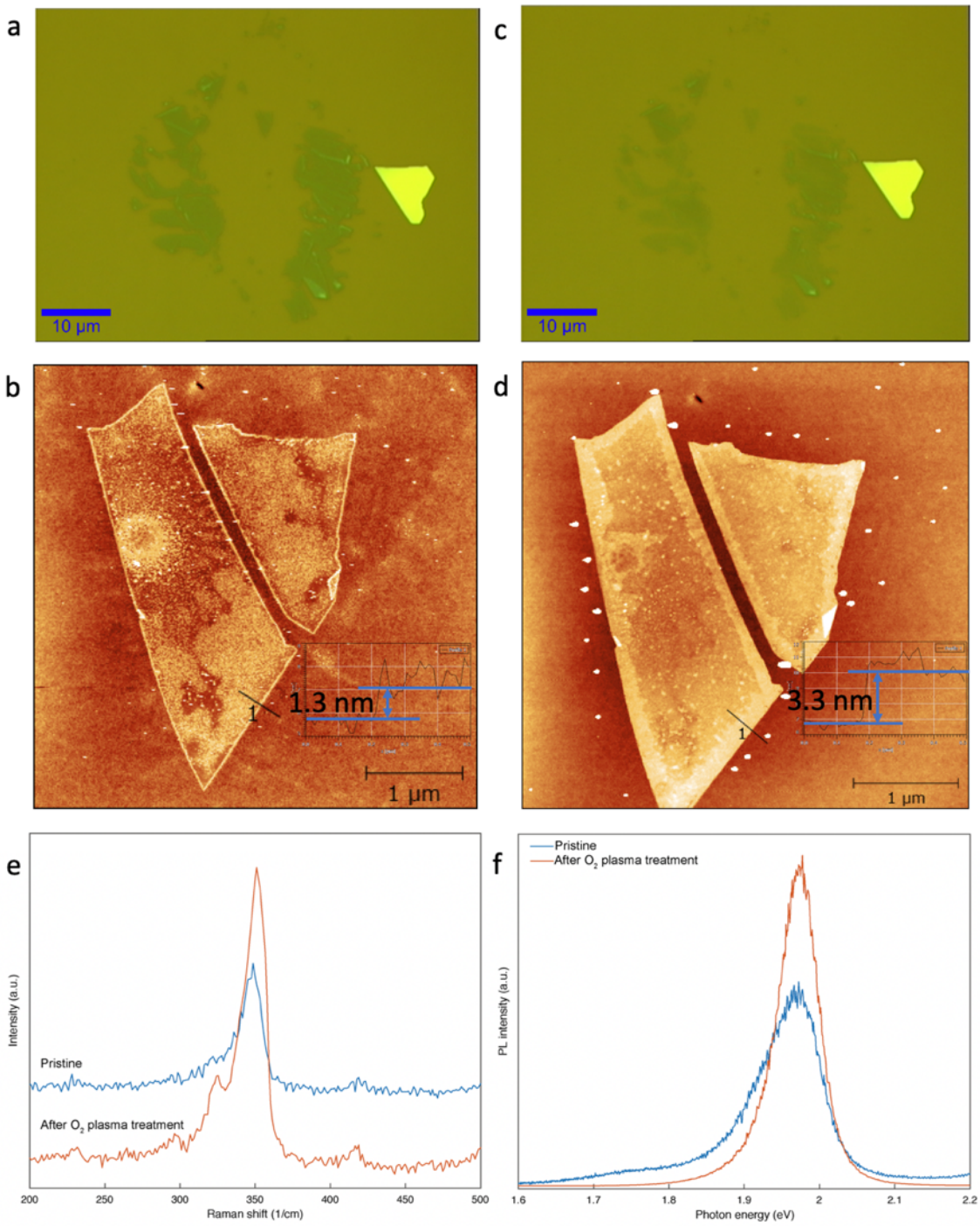

Figure 5-2: Mechanically Exfoliated Monolayer WS_2 2s O_2 Plasma Treatment. (a)&(c) Optical image of before and after the treatment. (b)&(d) AFM image of before and after treatment, showing an increase of flake thickness and smoothness. (e)-(f) The single spectrum of Raman shift and PL response, both showing that the treatment increased the intensities response, indicating a structure with lesser defects.

5.2 Air Plasma

5.2.1 MoS_2

In Fig 5-3(a) and (c), after 2 seconds of air plasma drastic difference of the disappearance of MoS_2 can be observed. This was assured by the result of the Raman and PL peak, Fig 5-3 (e)-(f), where the characteristic peaks of MoS_2 were basically gone. However, it is good to notice that from 200 to 350 cm^{-1} a hunch was formed with a new peak at 298 cm^{-1}. This indicates that there is new type of molecule interaction in the structure. According to Chu's finding, the peak can be referred to the vibration from MoO_3.[11] Hence, these nanoscrolls are most likely to be transition metal oxide (TMO) scrolls.

Moreover, if further comparison was made with this result with the O_2 plasma treated MoS_2, where MoS_2 signature Raman peaks were still visible and no scrolling response were documented. It can be concluded that oxidation of the flake is highly related to the forming of nanaoscroll. Which from Chu et al., the scrolling mechanism was originated from the structural difference of the upper layer and lower layer of the sandwich structure of TMDC structure. The upper layer that was oxidized will change from the longer Mo-S bond into shorter Mo-O bond. Hence, the strain induces the structure to start this self-propagating scrolling mechanism.

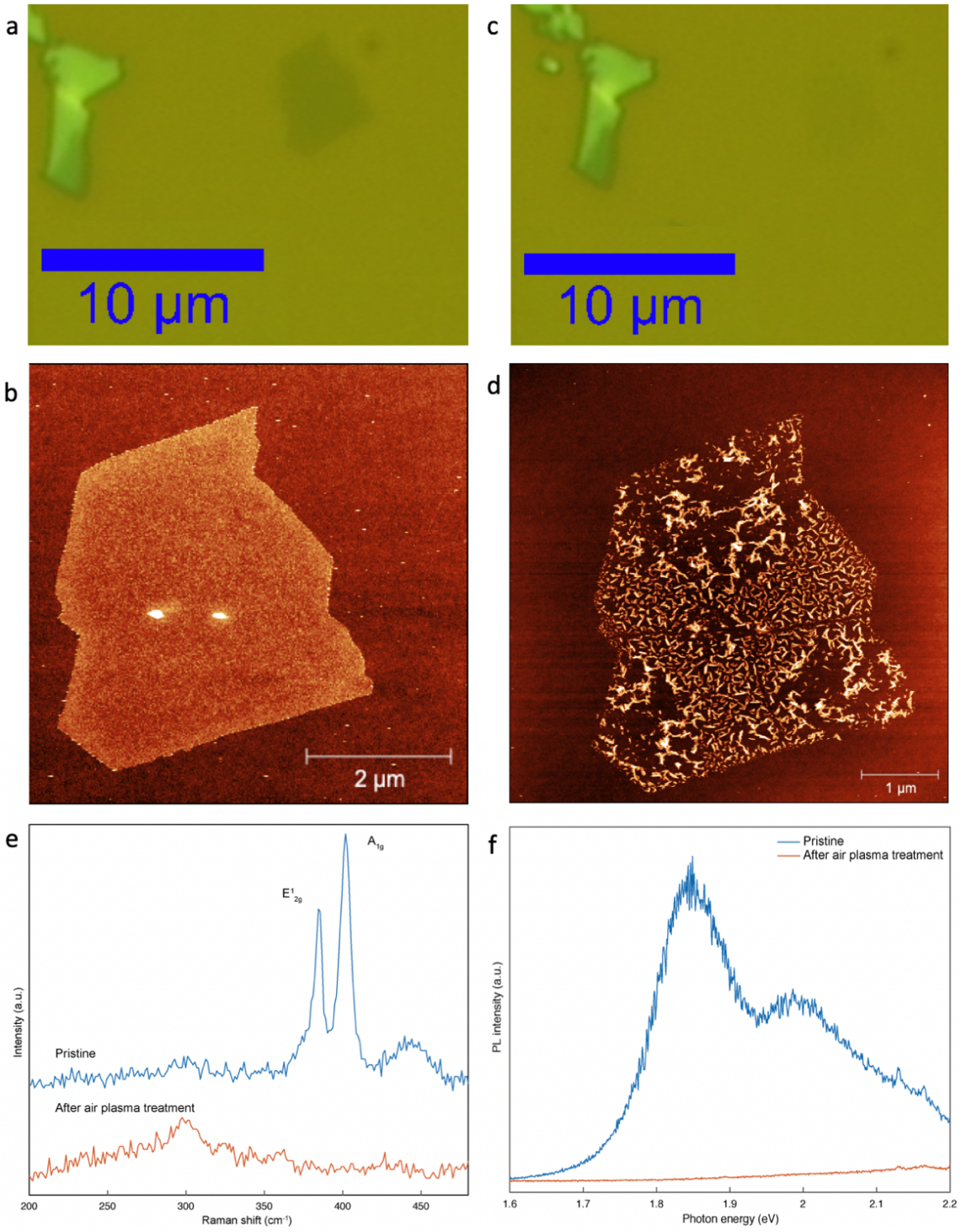

Figure 5-3: Mechanically Exfoliated Monolayer MoS_2 2s Air Plasma Treatment. (a)&(c) Optical images showing the flake was almost invisible after the treatment (b)&(d) AFM image of before and after treatment, where the flake was totally transformed into nanoscrolls. (e) The single spectrum of Raman shift where after the treatment, the character peaks of MoS_2 were gone and the peak indicating oxidation at 329 cm^{-1} appeared. (d) The single spectrum of the PL spectroscopy showing that the intensity was relaxed by the treatment.

5.2.2 WS_2

For WS_2 single-crystal, after both 2- and 4-seconds air plasma treatment, reaching the degree where the Raman signature peaks of WS_2 were gone. There were no new Raman shift peaks that indicate oxidation, nor any scrolling mechanism observed in AFM.

Comparing the result between Fig 5-4 and Fig 5-5, the longer the WS_2 was treated by the air plasma, the more distinct the change can be observed. First, for the optical change, in the 4s treatment, the flake is almost gone compare to the 2s which the flake can still be clearly seen, Fig 5-4 (b) and Fig 5-5 (b). Next, a trend of smoothing of the flake surface can be identified through both the AFM images, Fig 5-4. In 2s, the edge where were assumed as the aggregate of WS_2 yet diffused to develop the flake will be smoothed by the air plasma; in 4s, the overall surface of the flake can be seen with rough white dots will be etched away with the plasma. Last, after 4s, the Raman Shift peak and PL response were totally extinguished compare to 2s with both the peaks red shifted and lowered.

So, from this experiment, it can be argued that WS_2 is more stable than MoS_2 when going through O_2 plasma bombardment. And on the edge of the flake where it is thicker, it can be deduced that they are loosely structured WS_2 aggregations active sites that were meant to be expanding the domain of the crystal, are prone to being etched away by the plasma.

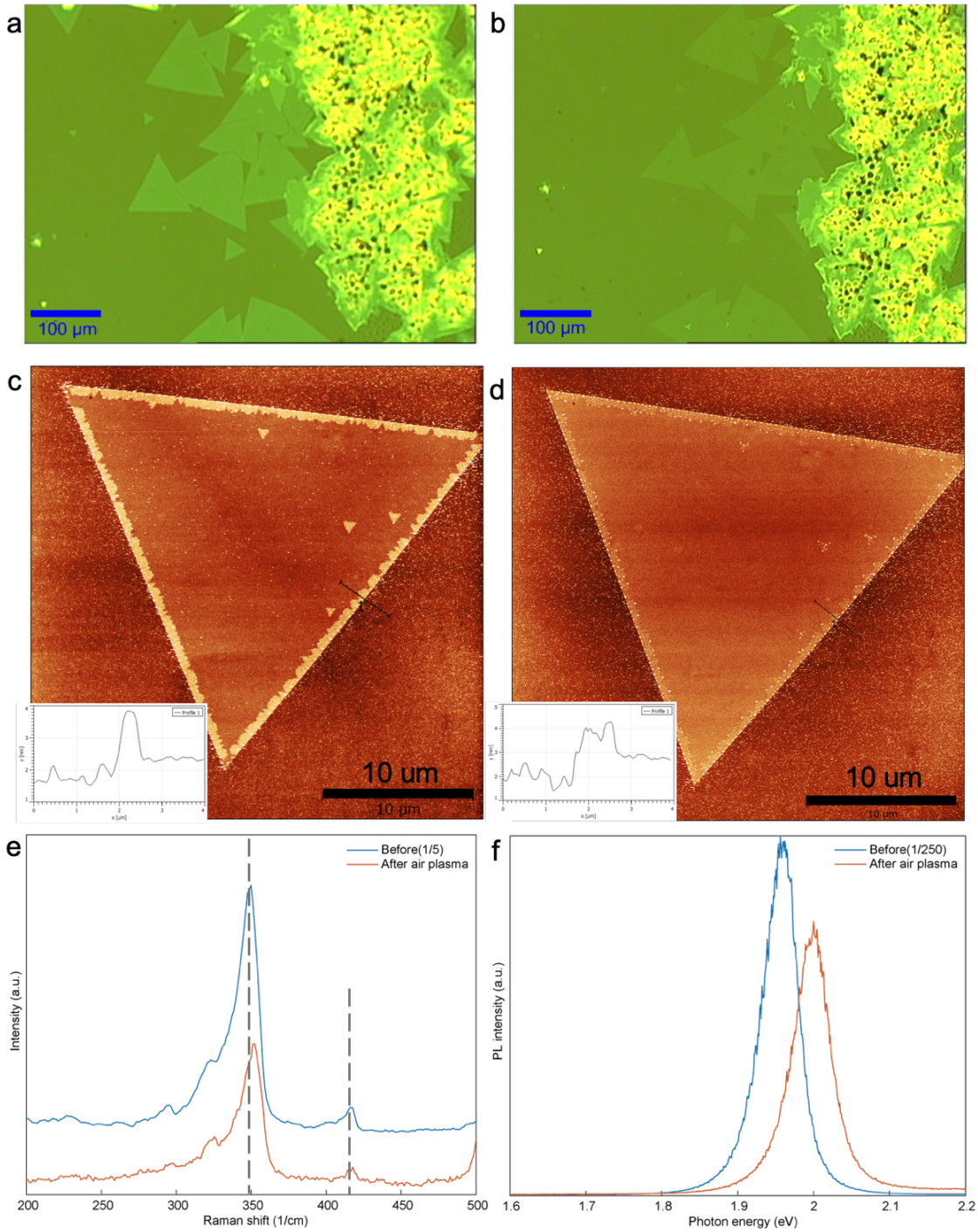

Figure 5-4: CVD grown WS_2 Single-Crystal with 2s Air Plasma treatment. (a)-(b) The optical image for the before and after treatment, with the flake becoming dimmer. (c)-(d) The AFM image comparison of the before and after, where the overall height was increased. (e),(f) The single spectrum of Raman shift and PL response, both indicating that the treatment decreased the intensities.

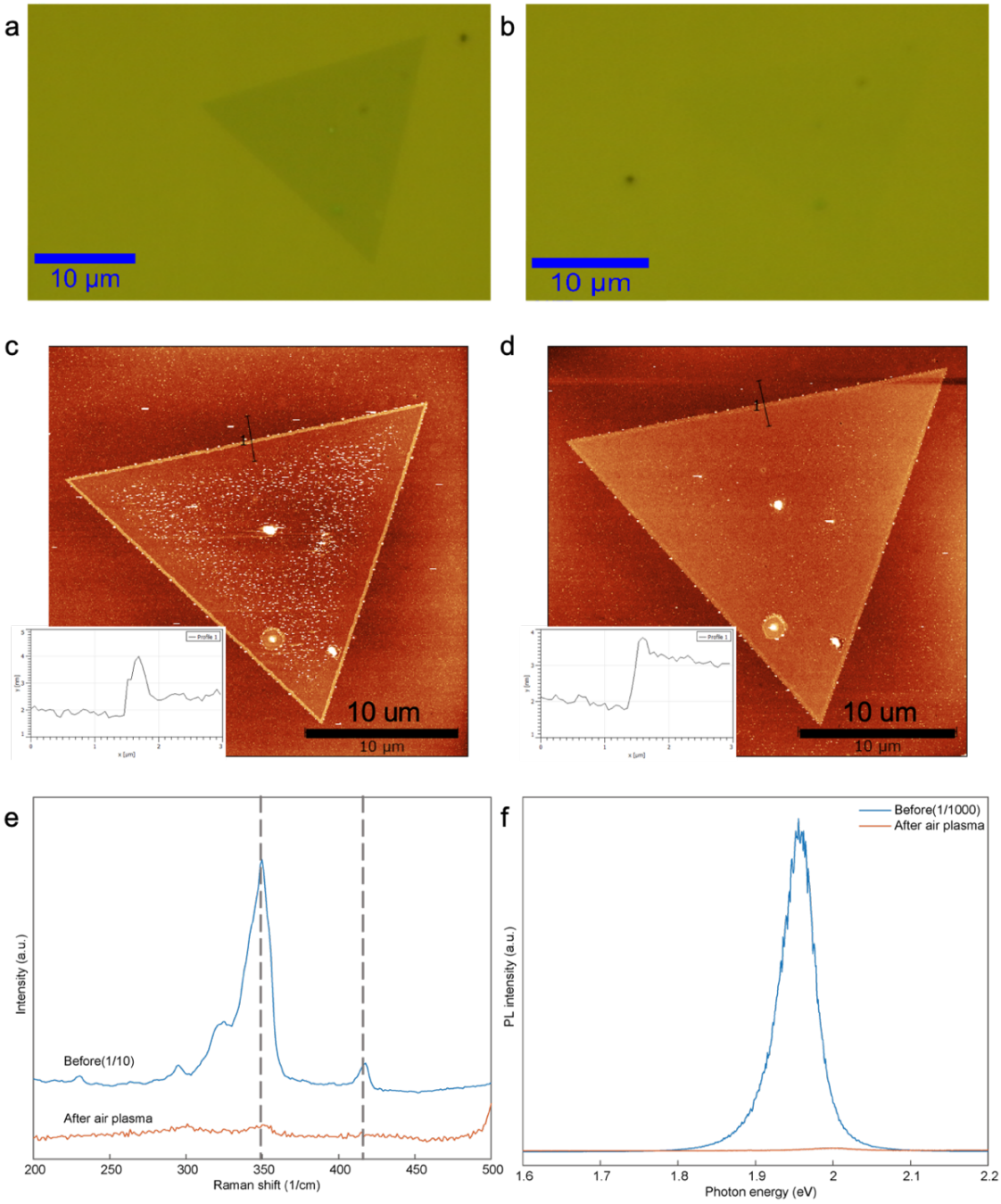

Figure 5-5: CVD grown WS_2 Single-Crystal with 4s Air Plasma treatment. (a)-(b) The optical image for the before and after treatment, with the flake becoming almost invisible. (c)-(d) The AFM image comparison of the before and after, where the overall height and the smoothness was increased (e)-(f) The single spectrum of Raman shift and PL response, both indicating that the treatment decreased the intensities.

5.2.3 Vertical Heterostructure

For the vertical heterostructure after 2s of air plasma treatment, the overall behavior lies the same as the outcome we got above. For the region where MoS_2 was exposed to the plasma, nanoscrolls and oxide Raman peaks could be found from Fig 5-6 (d) and (e) respectively. And for the heterostructure region where WS_2 covered MoS_2, there were no obvious morphology changes under AFM image. However, from several ratio from the Raman spectrum there are changes indicating the subtle changes in the structure. First, the intensity ratio of the A_{1g} and E^1_{2g} of MoS_2 (I_{A1g}/I_{E12g}) stayed the same, indicating that the MoS_2 structure were stable. On the contrast, the intensity ratio of the A_{1g} and E^1_{2g} of WS_2 (I_{A1g}/I_{E12g}) decreased, stating that the WS_2 region got thicker. Last, both the intensity ratio of out-of-plane vibration (E^1_{2g}) and in plane vibration(A_{1g}) of WS_2 to MoS_2 (I_{WS2}/I_{MoS2}) had increased, showing that the defects that the plasma introduced into WS_2 loosen up the structure. In a nutshell, for the vertical heterostructure, from the result we learnt that the top layer will serve as a shield for the underlying flake and the total PL response will decrease from the defects introduced to the structure.

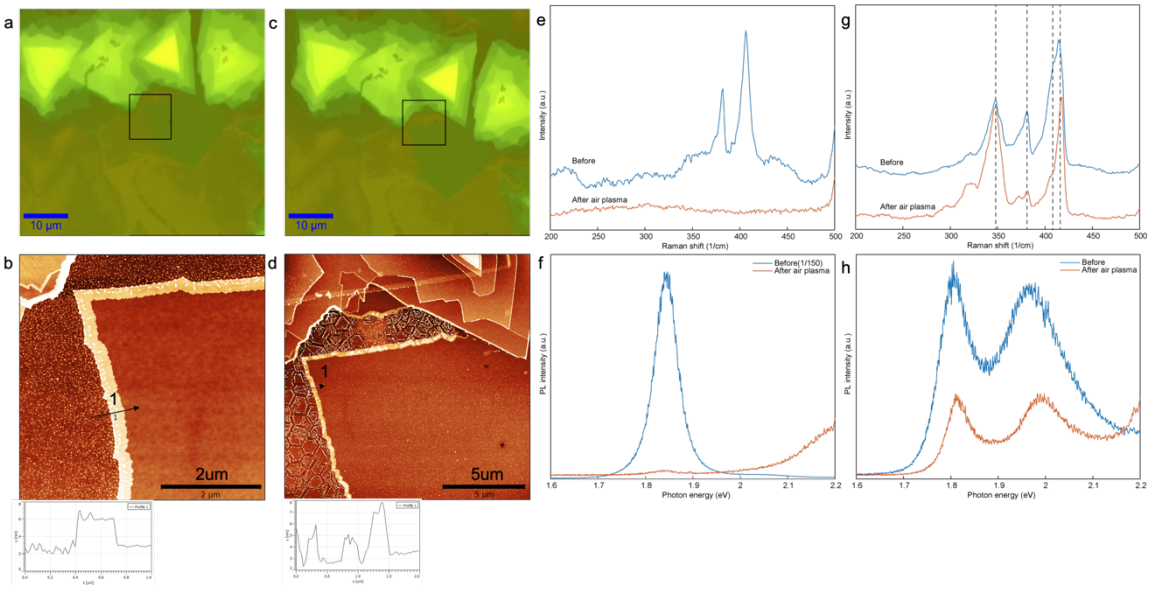

Figure 5-6: The Vertical MoS_2/WS_2 Heterostructure with 2s of Air Plasma. (a), (c) the optical image of the before and after treatment, showing some of the MoS_2 were etched away by the plasma. (b), (d) The detailed AFM image showing that the bare MoS_2 start forming cracks and nanoscrolls in hexagonal shape. But for the heterostructure part apart from becoming thicker, the overall outcome was the same. (e)-(f) Single spectrum of Raman and PL for MoS_2, where both the intensities were relaxed. (g)-(h) Single Raman and PL spectrum for heterostructure where the dotted line indicates the characteristic peaks for MoS_2 and WS_2. Both the intensities were quenched after the treatment.

5.2.4 Lateral Heterostructure

For the lateral heterostructure, unlike heterostructure, the whole system will be exposed to the air plasma. As a result, the defect will be distributed throughout the flake. Hence, the Raman and PL spectrum for both the TMDC will be significantly quenched. What is interesting for this result is that in the center where the MoS_2 is formed, after the treatment, although it showed oxidation Raman peak, only tiny cracks without nanoscrolls were formed. Furthermore, when approaching the boundary of MoS_2 and WS_2, the crack stopped forming. We assume the reason of the formation of this crack distribution gradient is because WS_2 is structurally more stable than MoS_2, in the region where they meet WS_2 will serve as a buffer to keep the doped/ oxidized MoS_2 in shape.

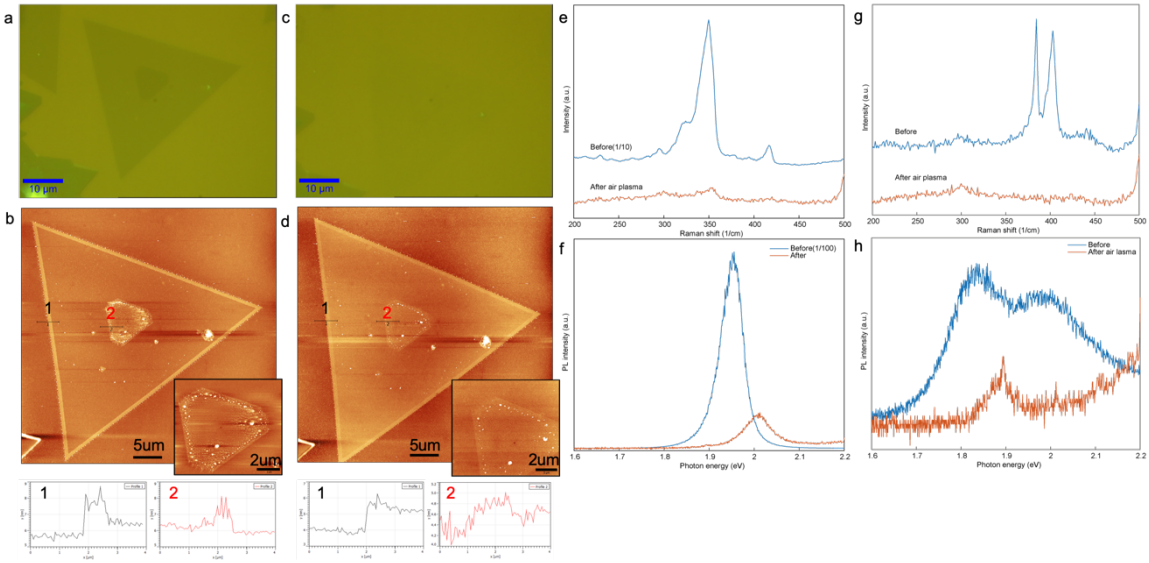

Figure 5-7: The Lateral MoS_2/WS_2 Heterostructure with 2s of Air Plasma. (a), (c) the optical image of the before and after treatment with the flake almost invisible post-treatment. (b), (d) The detailed AFM image showing that the overall thickness of the structure was increased. And through the inset pictures, which is the MoS_2 area, after the treatment the roughness of the region is lower but encompasses subtle cracks. (e)-(f) Single spectrum of Raman and PL for WS_2, where both the intensities were relaxed. (g)-(h) Single Raman and PL spectrum for MoS_2 where both the intensities were relaxed with an increase of the oxidation peak.

CHAPTER 6

CONCLUSIONS AND FUTURE WORK

6.1 Conclusion

In summary, in this project we demonstrated methods for growing large-area monolayer MoS_2, WS_2, and MoS_2/WS_2 heterostructure films on SiO_2/Si substrates via atmospheric pressure chemical vapor deposition (APCVD). And investigated how different plasma will affect the chemical and physical property of the flake, like formation of nanoscrolls.

First, for the as-grown monolayer MoS_2 films, they display good optical properties with semiconducting properties and a direct bandgap of ~1.84 eV. Moreover, the out-of-plane (A_{1g}), in-plane (E^1_{2g}) vibrations modes, and the resulting the difference(Δ) value to be 20.7 cm^{-1} also proved it is a monolayer single-crystal. The results of Raman characterization, PL intensity mapping, and AFM imaging indicate the monolayer MoS_2 is uniform in micro-scale. Secondly, the WS_2 films, after overcoming the precursor problem with the use of $WO_{2.9}$/NaCl mixture, the growth result not only shows good optical properties with semiconducting properties and a direct bandgap of ~1.95 eV, we also demonstrate the ability to scale up and manufacture them as large as ~200 μm in size. And by combining the Raman, PL, and AFM characterizations the process for this growth has proven itself to be well established. Last, for the MoS_2/WS_2 heterostructure films, by combining both the experiences acquired from the previous growths, well defined vertical and lateral heterostructures can be found.

In addition to CVD growth, O_2 and air plasma treatment on the films were demonstrated. First, the individual plasma treatment separately on MoS2 and WS_2, we found that overall WS_2 has a more stable structure. Because under the same exposure time of 2 seconds air plasma, MoS_2 will be oxidized and formed nanoscrolls. On contrast, even if WS_2 went through 4 seconds of treatment and lost its Raman signature and PL peaks, the flake will still be free of nanoscrolls. Second, when we work on vertical and lateral heterostructures the results are different. For vertical heterostructure, where WS_2 covers MoS_2, WS_2 will serve as a shield minimizing oxidation effect on MoS_2. As for lateral heterostructure, where MoS_2 is in the center and surrounded by WS_2, after the

bombardment of plasma, the WS_2 will serve as a frame to stop the propagation of the crack from MoS_2, making both free from forming nanoscrolls.

6.2 Future Work

For starter, the generation of the different types of exciton and its corresponding photoluminescence response resulting in the segmentation of in different samples need to be more investigated with different angles. For example, the employment of the absorption spectrum like FTIR, UV-Vis can help to understand how the different spots on the crystal absorbs the light and whether they are related to the intensity response. Also, the elemental characterization for the heterostructures will be needed to further confirm the formation of the different zone to help shine light onto formation anomalies.

Next, having the nanoscrolls formed for MoS_2 and not WS_2 meaning that the true mechanism is still not clear. To further understand, longer exposure of air plasma on the structure need to be employed. In addition to that, more characteristic methods need to be incorporated to understand the reaction. One of it will be the need of elemental analysis, like XPS to confirm the appearance of oxidation. As well as structural characterization, like transmission electron microscopy, to see how the atoms are aligned and the influence from the plasma treatment.

Moreover, studying the orientations of the crystals, the effect of using different substrate, and the methods to control the lengths, domain, and distributions of nanoscrolls will be needed to develop use. To standardize this quick way in synthesizing high surface-to-volume ratio of TMO nanosrolls could have future applications in nanoelectronic devices and as electrocatalyst.

REFERENCES

1. Geim, A. K. & Grigorieva, I. V. Van der Waals heterostructures. *Nature* **499**, 419–425 (2013).

2. Wang, Q. H., Kalantar-Zadeh, K., Kis, A., Coleman, J. N. & Strano, M. S. Electronics and optoelectronics of two-dimensional transition metal dichalcogenides. *Nature Nanotechnology* **7**, 699–712 (2012).

3. Zhu, H. *et al.* Observation of piezoelectricity in free-standing monolayer MoS 2. *Nat. Nanotechnol.* (2015). doi:10.1038/nnano.2014.309

4. Fontana, M. *et al.* Electron-hole transport and photovoltaic effect in gated MoS2 schottky junctions. *Sci. Rep.* (2013). doi:10.1038/srep01634

5. Fiori, G. *et al.* Electronics based on two-dimensional materials. *Nature Nanotechnology* (2014). doi:10.1038/nnano.2014.207

6. Li, H. *et al.* Fabrication of single- and multilayer MoS 2 film-based field-effect transistors for sensing NO at room temperature. *Small* **8**, 63–67 (2012).

7. Huo, N. *et al.* Novel and enhanced optoelectronic performances of multilayer MoS2 -WS2 heterostructure transistors. *Adv. Funct. Mater.* **24**, 7025–7031 (2014).

8. Nan, H. *et al.* Producing air-stable InSe nanosheet through mild oxygen plasma treatment. *Semicond. Sci. Technol.* **33**, 074002 (2018).

9. Nan, H. *et al.* Improving the electrical performance of MoS2 by mild oxygen plasma treatment. *J. Phys. D. Appl. Phys.* **50**, 154001 (2017).

10. Shim, J. *et al.* High-Performance 2D Rhenium Disulfide (ReS2) Transistors and Photodetectors by Oxygen Plasma Treatment. *Adv. Mater.* **28**, 6985–6992 (2016).

11. Chu, X. S., Li, D. O., Green, A. A. & Wang, Q. H. Formation of MoO3 and WO3 nanoscrolls from MoS2 and WS2 with atmospheric air plasma. *J. Mater. Chem. C* **5**, 11301–11309 (2017).

12. Radisavljevic, B., Radenovic, A., Brivio, J., Giacometti, V. & Kis, A. Single-layer MoS2 transistors. *Nat. Nanotechnol.* **6**, 147–150 (2011).

13. Cao, T. *et al.* Valley-selective circular dichroism of monolayer molybdenum disulphide. *Nat. Commun.* **3**, (2012).

14. Kuc, A., Zibouche, N. & Heine, T. Influence of quantum confinement on the electronic structure of the transition metal sulfide TS2. *Phys. Rev. B - Condens. Matter Mater. Phys.* **83**, 245213 (2011).

15. Koma, A. Van der Waals epitaxy for highly lattice-mismatched systems. *J. Cryst. Growth* (1999). doi:10.1016/S0022-0248(98)01329-3

16. Gurarslan, A. *et al.* Surface-energy-assisted perfect transfer of centimeter-scale monolayer and few-layer MoS2 films onto arbitrary substrates. *ACS Nano* **8**, 11522–11528 (2014).

17. Li, S. *et al.* Halide-assisted atmospheric pressure growth of large WSe2 and WS2 monolayer crystals. *Appl. Mater. Today* **1**, 60–66 (2015).

18. Hong, X. *et al.* Ultrafast charge transfer in atomically thin MoS 2 /WS 2 heterostructures. *Nat. Nanotechnol.* **9**, 682–686 (2014).

19. Liu, Y. *et al.* Layer-by-Layer Thinning of MoS $_2$ by Plasma. *ACS Nano* **7**, 4202–4209 (2013).

20. Nan, H., Zhou, R., Gu, X., Xiao, S. & (Ken) Ostrikov, K. Recent advances in plasma modification of 2D transition metal dichalcogenides. *Nanoscale* **11**, 19202 (2019).

21. Benetoli, L. O. de B., Cadorin, B. M., Postiglione, C. da S., Souza, I. G. de & Debacher, N. A. Effect of temperature on methylene blue decolorization in aqueous medium in electrical discharge plasma reactor. *J. Braz. Chem. Soc.* **22**, 1669–1678 (2011).

22. Takamatsu, T. *et al. Investigation of Reactive Species in Various Gas Plasmas Treated Liquid and Sterilization Effects*.

23. Amara, K. K., Chu, L., Kumar, R., Toh, M. & Eda, G. Wet chemical thinning of molybdenum disulfide down to its monolayer. *APL Mater.* **2**, 092509 (2014).

24. Islam, M. R. *et al.* Tuning the electrical property via defect engineering of single layer MoS 2 by oxygen plasma. *Nanoscale* **6**, 10033–10039 (2014).

25. Mitoraj, M. P. & Michalak, A. On the asymmetry in molybdenum-oxygen bonding in the MoO 3 structure: ETS-NOCV analysis. *Struct. Chem.* **23**, 1369–1375 (2012).

26. Kang, K. N., Godin, K. & Yang, E.-H. The growth scale and kinetics of WS2 monolayers under varying H2 concentration. *Sci. Rep.* **5**, 13205 (2015).

27. Liu, P. *et al.* Large-Area WS2 Film with Big Single Domains Grown by Chemical Vapor Deposition. *Nanoscale Res. Lett.* **12**, 558 (2017).

28. Castellanos-Gomez, A. *et al.* Deterministic transfer of two-dimensional materials by all-dry viscoelastic stamping. *2D Mater.* **1**, 011002 (2014).

29. Wang, Z. *et al.* NaCl-assisted one-step growth of MoS 2 -WS 2 in-plane heterostructures. *Nanotechnology* **28**, 325602 (2017).

30. Meitl, M. A. *et al.* Transfer printing by kinetic control of adhesion to an elastomeric stamp. *Nat. Mater.* **5**, 33–38 (2006).

31. Nečas, D. & Klapetek, P. Gwyddion: An open-source software for SPM data analysis. *Central European Journal of Physics* **10**, 181–188 (2012).

32. Ohring, M. *The Materials Science of Thin Films*. *The Materials Science of Thin Films* (2013). doi:10.1016/C2009-0-22199-4

33. Van der Vlies, A. J., Kishan, G., Niemantsverdriet, J. W., Prins, R. & Weber, T. Basic reaction steps in the sulfidation of crystalline tungsten oxides. *J. Phys. Chem. B* **106**, 3449–3457 (2002).

34. Schmidt, P., Binnewies, M., Glaum, R. & Schmidt, M. Chemical Vapor Transport Reactions–Methods, Materials, Modeling. in *Advanced Topics on Crystal Growth* (2013). doi:10.5772/55547

35. Boscher, N. D., Carmalt, C. J., Palgrave, R. G. & Parkin, I. P. Atmospheric pressure chemical vapour deposition of SnSe and SnSe2 thin films on glass. *Thin Solid Films* **516**, 4750–4757 (2008).

36. Lee, C. *et al.* Anomalous lattice vibrations of single- and few-layer MoS2. *ACS Nano* **4**, 2695–2700 (2010).

37. Coehoorn, R., Haas, C. & De Groot, R. A. Electronic structure of MoSe2, MoS2, and WSe2. II. The nature of the optical band gaps. *Phys. Rev. B* **35**, 6203–6206 (1987).

38. Splendiani, A. *et al.* Emerging photoluminescence in monolayer MoS 2. *Nano Lett.* **10**, 1271–1275 (2010).

39. Mak, K. F., Lee, C., Hone, J., Shan, J. & Heinz, T. F. Atomically thin MoS2: A new direct-gap semiconductor. *Phys. Rev. Lett.* **105**, (2010).

40. Baek, S. H., Choi, Y. & Choi, W. Large-Area Growth of Uniform Single-Layer MoS2 Thin Films by Chemical Vapor Deposition. *Nanoscale Res. Lett.* **10**, 388 (2015).

41. Berkdemir, A. *et al.* Identification of individual and few layers of WS2 using Raman Spectroscopy. *Sci. Rep.* **3**, 1755 (2013).

42. Cong, C. *et al.* Synthesis and optical properties of large-area single-crystalline 2D semiconductor WS2 monolayer from chemical vapor deposition. *Adv. Opt. Mater.* **2**, 131–136 (2014).

43. Peimyoo, N. *et al.* Nonblinking, intense two-dimensional light emitter: Monolayer WS 2 Triangles. *ACS Nano* **7**, 10985–10994 (2013).

44. Fu, Q. *et al.* Controllable synthesis of high quality monolayer WS 2 on a SiO 2 /Si substrate by chemical vapor deposition. *RSC Adv.* **5**, 15795–15799 (2015).

45. Yu, Y. *et al.* Equally efficient interlayer exciton relaxation and improved absorption in epitaxial and nonepitaxial MoS2/WS2Heterostructures. *Nano Lett.* **15**, 486–491 (2015).

46. Gong, Y. *et al.* Vertical and in-plane heterostructures from WS2/MoS2 monolayers. *Nat. Mater.* **13**, 1135–42 (2014).

47. Ji, Q., Zheng, Y., Zhang, Y. & Liu, Z. Chemical vapour deposition of group-VIB metal dichalcogenide monolayers: Engineered substrates from amorphous to single crystalline. *Chemical Society Reviews* **44**, 2587–2602 (2015).

49